Review Vol. 12, No. 9 / 1 Sep 2022 / Optical Materials Express 3327

Optical Materials EXPRESS

Ultrafast laser nanostructuring in transparent materials for beam shaping and data storage [Invited]

YUHAO LEI,* HUIJUN WANG, GHOLAMREZA SHAYEGANRAD, AND PETER G. KAZANSKY

Optoelectronics Research Centre, University of Southampton, Southampton, SO17 1BJ, United Kingdom
**yuhao.lei@soton.ac.uk*

Abstract: We review recent progress in femtosecond laser anisotropic nanostructuring of transparent materials, including silica glass and thin films. With different writing parameters, oblate nanopores, single lamella-like structures and nanoripples are demonstrated, which can be used in geometric phase optical elements, space variant polarization converters and multiplexed optical data storage.

1. Introduction

The interaction of intense ultrashort light pulses with transparent materials is of considerable interest due to observation of new physical phenomena and a wide range of applications in laser surgery [1], three-dimensional integrated optics [2–5], microfluidics [6,7], direct printing of optical elements [8,9] and optical data storage [10]. The key advantage of using femtosecond pulses for direct laser writing, as opposed to longer pulses, is that the energy can be rapidly and precisely deposited in solids [11,12]. The light is absorbed, and optical excitation ends before the surrounding lattice is perturbed, leading to highly localized nanostructures without collateral damage. Polarization controlled nanogratings can be fabricated by femtosecond laser writing in various bulk and thin-film transparent materials and silica glass in particular [13,14]. Under multi-pulse irradiation and certain conditions, laser-induced periodic surface structures (LIPSS) [15,16] can be observed on virtually any type of material such as metals [17–19], semiconductors [20,21], dielectric bulks [22–24] and thin films [25–27]. LIPSS can be divided into two categories according to spatial period. The classical LIPSS with the period of near wavelength is called low spatial frequency LIPSS (LSFL). In addition, the nanostructures with periods significantly smaller than the irradiation wavelength are termed high spatial frequency LIPSS (HSFL), or sometimes nanoripples/nanogratings. Nanoripples induced by femtosecond laser pulses on transparent thin films can be used for birefringence patterning [28,29], while LSFL cannot be utilized due to the lack of form birefringence in the visible range. Unlike LIPSS on almost any material, self-assembled lamella structures (nanogratings) can be only produced inside a number of transparent glass [13,30–35] or crystals [36–39]. Self-assembled nanogratings in silica glass written by femtosecond laser pulses has been used for different applications due to their controllable optical anisotropy and high durability [13,40].

One application of nanogratings in transparent materials is the fabrication of geometric phase (GP) elements and space variant polarization converters. The geometric phase, also known as the Pancharatnam-Berry phase [41,42], shift has emerged as a promising method to control light with spatially variant anisotropy rather than optical path difference. For instance, after transmitted through a half-wave plate, the handedness of the circularly polarized beam is flipped and an additional phase shift is added, which is proportional to twice of the rotation angle of the waveplate [43]. By spatial patterning the slow axis of birefringence, desired phase profile can be realized to construct lenses, gratings or holograms, and the theoretical efficiency is

#463151
Journal © 2022

https://doi.org/10.1364/OME.463151
Received 6 May 2022; revised 24 Jun 2022; accepted 27 Jun 2022; published 2 Aug 2022

almost 100% by means of the GP [43–45]. On the other hand, birefringence patterning has been used to generate vector light beams, in which the polarization varies in different local positions [46]. Vector beams have many interesting applications in fundamental sciences [47,48]. For instance, a radial polarized beam allows the focusing of light below the diffraction limit [49], due to its non-vanishing longitudinal electric field component. Besides, azimuthal vector beams with longitudinal magnetic fields [50] have great potential in spectroscopy and microscopy. Fabrication of geometric phase optical elements (GPOE) has been demonstrated by thin plasmonic meta-surfaces by the lithographic method [51]. However, how to achieve meta-surface with high transmission and efficiency remains a challenge. The alternative solution is photoalignment of liquid crystals [44,52], but high absorption in the ultraviolet (UV) and infrared (IR) ranges and low durability prevent their applications. GPOEs and vector beam converters with high durability and optical damage threshold have been fabricated by local manipulation of nanogratings and associated form birefringence in silica glass [53,54], but its low transmission, especially in the visible and ultraviolet range, prevents their applications.

Another application of nanogratings by femtosecond laser writing in silica glass is multiplexed optical data storage with the merits of a virtually eternal lifetime and high capacity [55]. The idea of optical recording based on fs laser writing was first proposed and demonstrated in photopolymers [10,56]. Later, three-dimensional (3D) optical data storage was realized in silica glass by tight focusing of femtosecond laser pulses [12,57]. The high-capacity optical recording was demonstrated by multiplexing new degrees of freedom including intensity, polarization, wavelength, and orbital angular momentum (OAM) by harnessing silver clusters embedded in glass [58] and plasmonic properties of metallic nanoparticles [59–62]. Polarization multiplexed data recording, also known as five-dimensional (5D) optical data storage, was implemented using self-assembled nanogratings generated by ultrafast laser writing in silica glass by means of the slow axis orientation (4th) and retardance (5th) in addition to three spatial coordinates [55,63,64].

Here, we review recent progress in low-loss smooth nanogratings [65] and ultralow-loss oblate nanopores [66] in silica glass as well as nanoripples in thin films [28,29] and their applications in optical elements for beam shaping. Besides, the advances in multiplexed optical data storage based on anisotropic nanopores [67] and single nanolamella-like structures [68] are presented, in which data writing speed and capacity have been improved.

2. Femtosecond laser writing setup

We used two different laser systems to cover a broad range of laser parameters. The experiments were carried out with a mode-locked Yb:KGW regenerative fs laser system (PHAROS, Light Conversion Ltd.), operating at a wavelength of 1030 nm and the second harmonic (515 nm) with a repetition rate from 200 kHz to 1 MHz and a pulse duration tuned in the range of 190–700 fs. The second laser system was a Yb-doped fibre fs laser (Satsuma, Amplitude), operating at 515 nm with a repetition rate of 10 MHz and a pulse duration of 250 fs. The laser beam was focused with an objective lens 170 μm below the surface of a silica glass substrate, which was mounted on an XYZ linear air-bearing translation stage (Aerotech Ltd.). The energy of the laser pulses was controlled by an attenuator and measured after the objective lens.

The modulation of the polarization direction of the laser beam is the key to imprinting controllable anisotropic nanostructures. The polarization direction of a linearly polarized beam can be continuously rotated by a half-wave plate mounted on a mechanical rotary stage, but it is difficult to rapidly obtain an arbitrary polarization azimuth. Although a spatial light modulator (SLM) can be used to achieve arbitrary polarization direction, the low refresh rate of around 100 Hz limits its application. Alternatively, an electro-optic modulator (EOM), i.e., a Pockels cell, with a modulation rate of MHz level can be employed for polarization modulation in femtosecond laser nanostructuring. For example, a combination of a polarizer, a Pockels cell, and a quarter-wave plate (Fig. 1) is used to control the polarization azimuth of a linearly polarized laser beam.

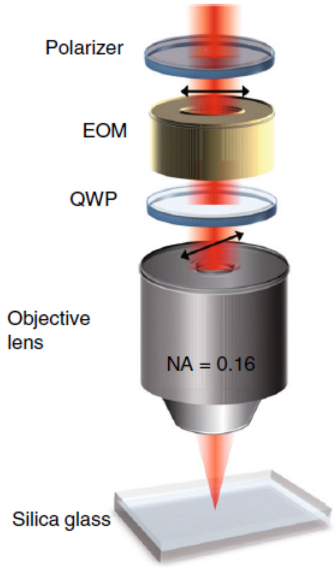

Fig. 1. Schematic of laser writing setup. EOM is an electro-optic modulator and QWP is a quarter-wave plate.

The retardance and slow axis orientation of laser-induced birefringent modifications were quantitatively analyzed with an Olympus BX51 optical microscope equipped with a birefringence measurement system (CRi Abrio imaging system) operating at 546 nm wavelength. The optical transmission spectra and phase change were measured with a VIS/NIR micro spectrometer (CRAIC) and a wavefront sensor (SID4-HR, Phasics), respectively. After lapping/polishing and etching with a KOH solution (1 mol/L) for 24 hours, the laser-modified region was imaged by a scanning electron microscope (SEM, Zeiss Evo50).

3. Nanostructuring by ultrafast laser

Depending on femtosecond laser fluence, three types of modification (Fig. 2) can be produced in the bulk of silica glass: isotropic refractive index increase (Type I) [69,70, 71], nanogratings (Type II) [55], and voids (Type III) [12,72]. Smooth positive refractive index change can be induced at a lower fluence, and the laser-written tracks can be used as waveguides in silica glass. Since no photosensitivity is required, waveguides can be fabricated in various materials with 3D complex geometries, which have been used in telecommunication [73], microfluidics [74] and quantum optics [75]. At much higher fluence, nanovoids surrounded by compacted materials are produced due to micro explosion when the absorbed energy density is higher than Young's modulus of material [72,76,77]. A single nanovoid can be produced by only one femtosecond laser pulse in various materials such as fused silica, quartz and sapphire [77]. In addition, a chain of well-organized nanovoids can be induced in transparent materials due to filament formation [78–80]. At a moderate fluence, self-assembled lamella structures, nanogratings, perpendicular to writing laser beam polarization are observed, which always acts as a negative uniaxial crystal [13,81,82]. The azimuth of the slow axis is perpendicular to the laser beam polarization and the typical birefringence of n_e-n_o is $-(2\text{-}4\times10^{-3})$. Besides, femtosecond laser pulses with different polarizations can erase and overwrite previously produced nanogratings, enabling type II modification as a rewritable optical medium [83, 84]. Although nanogratings in silica glass have advantages of high thermal durability and optical damage threshold [85,86], high transmission loss and low throughput hinder their applications. Herein, starting from conventional nanogratings, we focus on recent progress in femtosecond laser anisotropic nanostructuring, including smooth nanogratings, oblate nanopores, single nanolamella-like structures, and nanoripples.

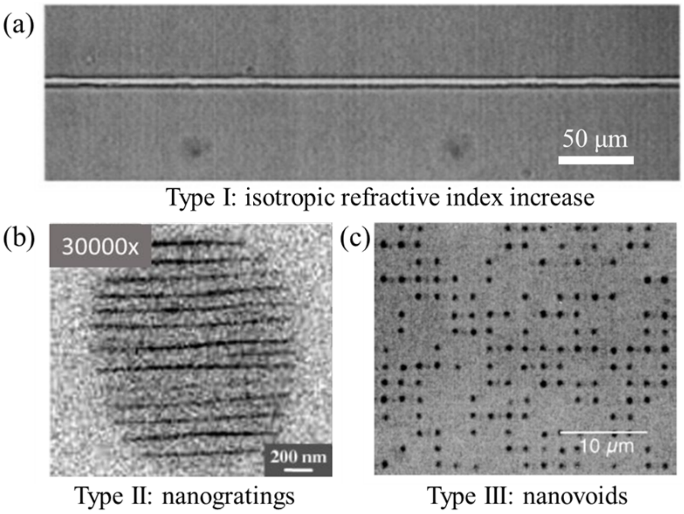

Fig. 2. Three types of fs laser induced modification inside silica glass: (a) isotropic refractive index increase (Type I). Reproduced with permission from [70] © 1997 American Institute of Physics; (b) nanogratings (Type II). Reproduced with permission from [13] © 2003 American Physical Society, and (c) voids (Type III). Reproduced with permission from [12] © 1996 Optica Publishing.

3.1. Smooth nanogratings (type II smooth)

Despite a number of nanogratings based optical elements have been demonstrated by femtosecond laser direct writing in silica glass, the efficiency of elements is lower than 70% in the visible range due to its low transmission. High-quality nanogratings were imprinted in silica glass by laser pulses (300 fs, 1030 nm, 200 kHz, 450 nJ, 1 mm/s) focused by a 0.35 NA objective lens (Fig. 3(a)). The transmission of a half-wave retarder at 532 nm is up to 90% (Fig. 3(b)), so the efficiency of a polarization grating is as high as 90%, which will be discussed in section 4. The dispersion analysis was performed from 440 nm to 680 nm, revealing the waveplate has a chromatic behavior.

3.2. Oblate nanopores with ultralow-loss (type X)

Nanograting based birefringent pattern with a retardance of 150 nm and a birefringence of 2.1 × 10^{-3} was imprinted by raster scanning writing with a line spacing of 1 μm (1030 nm, 300 fs, 0.7 μJ, 200 kHz, 1 mm/s corresponding to 200 pulses/μm), which can be clearly observed under a transmitted light microscope (Fig. 4(a)). In contrast, ten layers of birefringent modification with high transmission were fabricated at a faster scanning speed of 6 mm/s, corresponding to 33 pulses/μm, to achieve the same retardance level (~150 nm), but they were almost invisible under a transmitted light microscope (Fig. 4(b)). The birefringence of ultralow-loss birefringent modification is 6×10^{-4}, which is one order of magnitude lower than that of the high-loss counterpart.

The transmission of high-loss and low-loss birefringent modification was measured from the UV to the NIR range for quantitative comparison (Fig. 4(c)). The transmission of high-loss

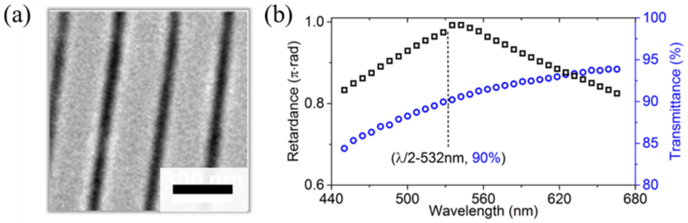

Fig. 3. (a) SEM image of smooth nanogratings. Processing conditions: 200 kHz repetition rate, 450 nJ pulse energy, 300 fs pulse duration, focusing via 0.35 NA lens, 1 mm/s scanning speed, 1 µm line spacing. Scale bar is 300 nm. (b) Phase retardation (□) and optical transmission (○) spectra of the imprinted half-wave retarder tuned for a 532 nm wavelength. Reproduced from [65] under CC BY 4.0.

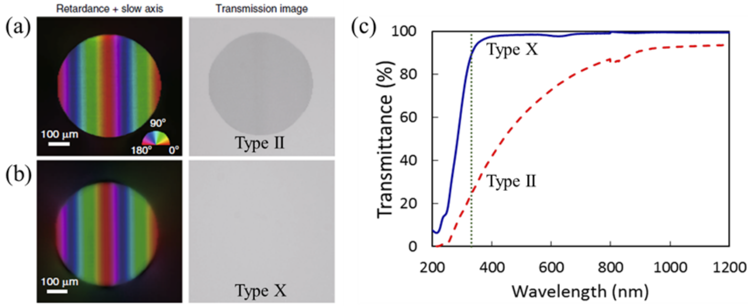

Fig. 4. Birefringence and optical microscope images of (a) high-loss and (b) low-loss birefringent structures. The colour scale indicates the slow axis orientation of the birefringence. (c) Transmission spectra of birefringent structures of high-loss type II (red dashed line) and low-loss type X (blue solid line) modifications with reference to pristine silica glass. The vertical dotted line indicates a wavelength of 330 nm, at which the transmission for the low-loss modification is 90%. Reproduced from [66] under CC BY 4.0.

nanograting modification rapidly decreases from 90% in the NIR range to just 30% in the UV range. By contrast, the transmission for low-loss modification was as high as 99% in a large range (400-2400 nm) and higher than 90% down to 330 nm. The transmission difference indicates the low-loss birefringent modification, referred to as type X, is fundamentally different from nanograting based high-loss birefringent modification.

SEM imaging of the low-loss and high-loss birefringent modification was carried out to reveal the evolution of nanostructures with different numbers of pulses (N_p) and corresponding birefringence and optical transmission images were presented for comparison (Fig. 5). For N_p=50, randomly distributed nanopores were observed and they were flatted perpendicular to the polarization of the writing laser beam (Fig. 5(a)), where the measured retardance was as small as ~1 nm. With a higher number of pulses (N_p=100-150), the concentration and the aspect ratio of nanopores increased, leading to a higher retardance of birefringent modifications. The nanopores were always flattened perpendicular to the polarization of the writing beam and the slow axis of birefringence was parallel to the elongation direction (Fig. 5(b)). The transformation from the low-loss modification to the high-loss one happened at N_p>200, where self-assembled nanoplanes appeared and the modification became visible under a transmitted light microscope (Fig. 5(c)). The SEM images suggest that the smaller nanostructure size is responsible for the lower transmission loss of type X modification.

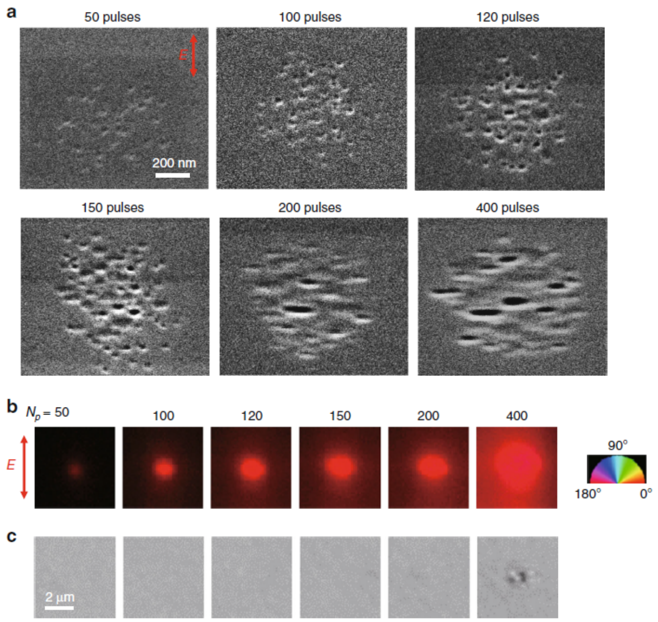

Fig. 5. Imaging of birefringent modifications written by different numbers of pulses. (a) SEM images of the polished surfaces of modifications written by laser irradiation (1030 nm, 300 fs, 0.7 µJ) with different pulse numbers (N_p). (b) and (c) Birefringence and optical transmission images of laser-induced modifications with different pulse numbers, respectively. Reproduced from [66] under CC BY 4.0.

The mechanism of polarization-controlled oblate nanopores formation should involve at least two processes: (1) generation of randomly distributed nanopores and (2) flatting of nanopores perpendicular to the polarization of the writing beam. The formation of nanopores implies the production of oxygen molecules inside silica glass after the irradiation by femtosecond laser pulses, whose relation between defects has been demonstrated in the literature [87–90]. In fact, the low-loss birefringent modification, oblate nanopores, cannot be observed for pulse durations shorter than 220 fs, indicating a time duration larger than a critical value is necessary for the formation of nanopores. One possible explanation is the interaction between light and self-trapped triplet excitons (STE), which could transform to transient defects pair of the E' centre and the non-bridging oxygen hole centre (NBOHC). Such transient defects pair can be generated within 250 fs after photoexcitation in fused silica [88].

$$\equiv \mathrm{Si}-\mathrm{O}-\mathrm{Si}\equiv \xrightarrow{250\,\mathrm{fs}} \equiv \mathrm{Si}\cdot + \cdot\mathrm{O}-\mathrm{Si}\equiv \tag{1}$$

where ≡Si· is E' center and ≡Si-O· is NBOHC. When the pulse duration is longer than 250 fs, the photoexcitation of NBOHC could happen due to multiphoton absorption or impact ionization by high energy electrons (~18 eV, two times of the silica glass band gap) generated during the avalanche ionization, leading to the dissociation of oxygen atom:

$$\equiv \mathrm{Si}\cdot + \cdot\mathrm{O}-\mathrm{Si}\equiv \xrightarrow{\mathbf{h}\nu\ \mathrm{or\ e}-} \equiv \mathrm{Si}^{+}\mathrm{Si}\equiv + \mathrm{O}^{0} + \mathrm{e}^{-} \tag{2}$$

where $\equiv\mathrm{Si}\cdot^{+}\mathrm{Si}\equiv$ is E_{δ}' center, O° is an interstitial oxygen atom and e- is an electron. Two oxygen atoms are essential to generate one oxygen molecules, which could facilitate nanopores formation in silica glass [91]. For pulse duration shorter than 250 fs, the probability of reaction (2) is reduced, so no type X modification is observed for $t_p < 220$ fs. The mechanism based on reaction

(2) is supported by the absorption (Fig. 6(a)) and photoluminescence (Fig. 6(b)) spectra of different modifications. Only NBOHCs are detected in the optically isotropic modification (type I) [92] and type X, but E_δ' centers are detected in the birefringent modifications (type X and type II), meaning that the generation of E_δ' centers is accompanied by the generation of oxygen atoms according to the reaction (2). The weak absorption band at ∼620 nm due to NBOHC in type X modification can be easily quenched by annealing at 400 °C for two hours (Fig. 6(c)) [87]. Besides, no type X modification was observed with NA > 0.50 and by photoexcitation for a 515 nm wavelength writing beam. The detailed mechanism is still under investigation and will be reported elsewhere.

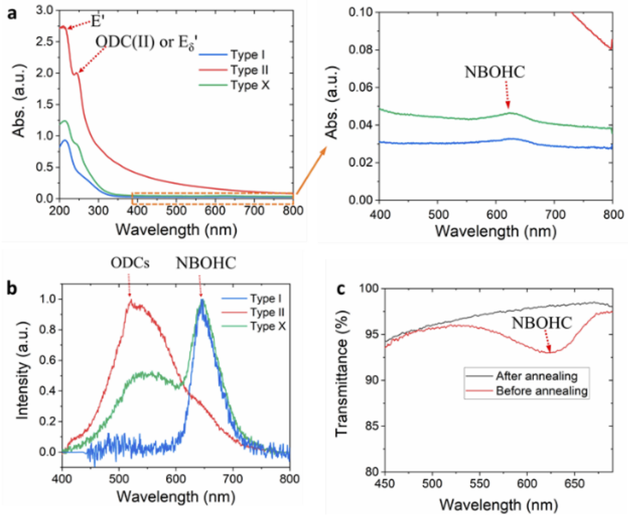

Fig. 6. (a) UV-VIS absorption spectra of different modifications in silica glass; (b) Photoluminescence spectra of different modifications with 343 nm laser excitation. (c) The absorption of the NBOHC before and after the annealing at 400 °C for two hours. Reproduced from [66] under CC BY 4.0.

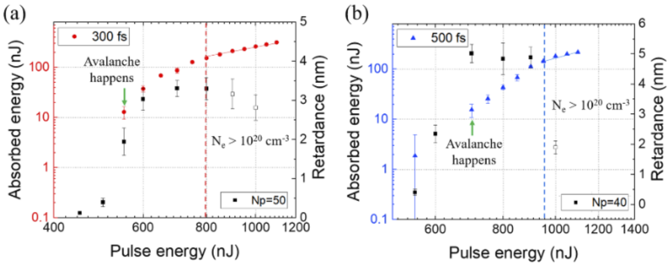

Fig. 7. Absorbed energy of single laser pulse and retardance of birefringent voxels versus pulse energy for pulse durations of (a) 300 fs and (b) 500 fs. Each voxel is written by 50 (40) pulses with duration of 300 (500) fs focused by a 0.16 NA lens. The solid and hollow black squares represent type X and type II modifications, respectively. Reproduced from [67] under CC BY 4.0.

To understand the energy deposition mechanism, the nonlinear transmission of a single pulse was measured for different pulse energies and durations at 1030 nm wavelength focused by a 0.16 NA lens. The sharp drop in the transmission from 100%, implying a fraction of energy is absorbed, is the signature of avalanche ionization. For a pulse duration of 300 fs, the avalanche ionization starts at a pulse energy of about 550 nJ (7.2 TW cm^{-2}) and dominates at 800 nJ (10.5 TW cm^{-2}) (Fig. 7(a)), and type X voxels were produced by 50 pulses for energies between 550 nJ and 800 nJ, while type II modification was imprinted above 800 nJ. This could indicate that moderate free electron concentration (N_e) of 10^{18}–10^{19} cm^{-3} [93,94] is responsible for the formation of flattened nanopores, where the pulse energy is just above the threshold of avalanche ionization. The higher free carrier density of about 10^{20} cm^{-3} generated by larger pulse energy is necessary for the formation of nanogratings (type II) [95,96]. Similar pulse energy dependence of birefringent modifications was observed for 500 fs pulses (Fig. 7(b)) and different pulse numbers.

3.3. Single nanolamella-like structure (type S)

In order to improve the throughput of laser nanostructuring, a high repetition rate femtosecond laser was used to write a group of voxels in silica glass by 30 nJ pulses with different repetition rates and number of pulses (Fig. 8). Birefringent dots with a slow axis perpendicular to the polarization direction of the writing beam were observed at the repetition rate of 1 MHz. However, voxels surrounded by strong stress were observed in the laser irradiated region due to heat accumulation for a repetition rate of 5 or 10 MHz. Reducing the laser spot size could prevent heat accumulation. The alternative solution is an efficient energy deposition, meaning more energy is utilized to modify rather than heat the material.

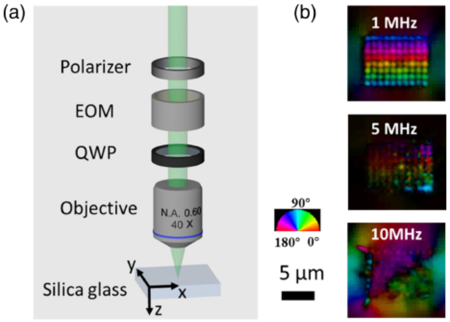

Fig. 8. Laser writing of birefringent structures inside silica glass. (a) Schematic of laser writing setup. EOM is an electro-optic modulator and QWP is a quarter-wave plate. (b) Images of the slow axis azimuth of voxels written by 100 laser pulses. Processing conditions: 515 nm wavelength, 250 fs pulse duration, 30 nJ pulse energy, and 0.6 NA objective lens. Pseudo-colors (inset) indicate the local orientation of the slow axis. Reproduced with permission from [68] © 2021 Optica Publishing.

More specifically, birefringent modifications consist of nanogratings or oblate nanopores can be imprinted by tens of fs laser pulses in silica glass, leading to high energy consumption. In contrast, a single pulse with absorbed energy density above Young's modulus of silica glass is able to produce a round shape nanovoid [12,75]. The following pulses with less energy could modify the shape of the nanovoid via near-field enhancement [97–99], which forms at the edge of a nanovoid and induces localized ionization to produce an anisotropic nanostructure without detrimental thermal accumulation.

In the experimental demonstration, two seeding pulses (E_s=32 nJ, 18.9 TW/cm^2, 3.6 J/cm^2) and eight writing pulses (E_w=14.4 nJ, 8.5 TW/cm^2, 1.6 J/cm^2) were focused inside the silica glass sample (Fig. 9(a), left). High-quality birefringent voxels with good reproducibility were imprinted with an average retardance of 2.6 nm and the azimuth of the slow axis perpendicular to the laser beam polarization. By contrast, modification with collateral damage occurred when writing with 10 pulses of 32 nJ energy (Fig. 9(a), middle-left). On the other hand, two seeding pulses of 32 nJ or 10 writing pulses of 14.4 nJ were not enough to produce detectable birefringence (Fig. 9(a), middle-right and right). The material temperature versus time was simulated at the center of the laser spot by the thermal diffusion equation [100]. The thermal accumulation was evident for the case without energy modulation, but the estimated temperature was reduced from 21,000 K to below 1,200 K by using of energy modulation method (Fig. 9(b)).

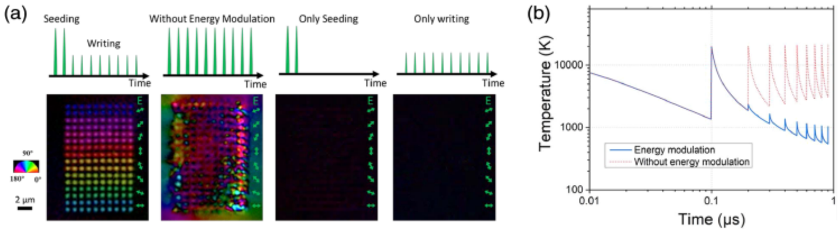

Fig. 9. Writing of birefringence structures via near-field enhancement with energy-modulated pulses. (a) Birefringence image of voxels written by two seeding pulses of 32 nJ and eight writing pulses of 14.4 nJ (left), ten pulses of 32 nJ (middle left), two seeding pulses of 32 nJ (middle right) and ten writing pulses of 14.4 nJ (right) with a repetition rate of 10 MHz, a pulse duration of 250 fs, and a wavelength of 515 nm. Pseudo-colors (inset) indicate the local orientation of the slow axis. The doubled arrows show the azimuth of polarization of the laser beam. (b) Simulated temperature evolution at the focus center versus time with and without energy modulation. Reproduced from [68] under CC BY 4.0.

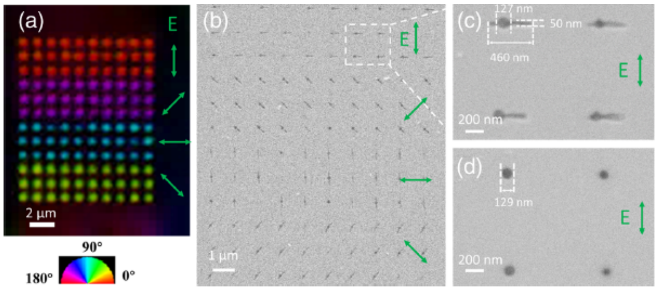

Fig. 10. Imaging of anisotropic nanostructures. (a) Image of the slow axis azimuth of voxels induced by two seeding pulses (E_S=36 nJ) and eight writing pulses (E_W=16.8 nJ) with a repetition rate of 500 kHz and the pulse duration of 190 fs at 515 nm wavelength. The pseudo-color represents the slow axis azimuth. (b) SEM image of the nanolamella-like structure after polishing and KOH etching; (c) enlarged area in the dashed square in (b); (d) SEM image of isotropic nanovoids created by two seeding pulses. The polarization direction (E) is indicated in the figure, and the laser beam propagation direction is perpendicular to the screen. Reproduced from [68] under CC BY 4.0.

Well-defined birefringent voxels with ~ 3.5 nm retardance were produced by two seeding pulses (E_s=36 nJ) and eight writing pulses (E_w=16.8 nJ) with a repetition rate of 500 kHz and pulse duration of 190 fs at 515 nm wavelength (Fig. 10(a)). Localized single nanolamella-like structures, referred to as type S, were observed in the SEM image and the orientation of the lamella structure was perpendicular to laser beam polarization (Fig. 10(b)). With only two seeding pulses, a 130 nm circular nanovoid was generated in the center of the photoexcited region (Fig. 10(c)) and then the nanolamella-like structure was produced by following writing pulses via near-field enhancement. The nanovoid was surrounded by a compact region due to laser induced microexplosion (Fig. 10(d)) and the estimated density is 1.10 ± 0.04 times higher than pristine silica glass [76]. The beam diameter of 1 μm was 7 times the diameter of the nanovoid (130 nm), suggesting the microexplosion happens only in the center of the photoexcited region because of multiphoton ionization (four photons of 2.4 eV for silica glass) and threshold effect. Such nanolamella like structures written by a few laser pulses at a high repetition rate enable high throughput of laser nanostructuring and are in particular beneficial for 5D optical data storage, which will be presented in section 5.

3.4. Nanoripples in thin films

In this section, we review the nanoripples formation on transparent films, such as indium tin oxide (ITO) film and amorphous silicon (a-Si) film, and their associated anisotropic properties. The 145 ± 10 nm thick ITO film was deposited on float glass by sputtering and nanoripples with a period of ~120 nm and a duty cycle of 10-20% of nanogrooves were produced after irradiation of femtosecond laser pulses (Fig. 11). The nanoripples were perpendicular to the polarization azimuth of the laser writing beam and the period was significantly smaller than the laser wavelength of 1030 nm. Nanostructures with such a small period (~λ/9) are termed high spatial frequency LIPSS (HSFL) or sometimes nanoripples, which is general after irradiation of ultrashort laser beam with a density of thousands of pulses per spot. Although the form birefringence of nanoripples on the ITO film is around -0.2, which is two orders of magnitude larger than that of nanogratings inside silica glass, the maximum retardance of nanoripples was about 45 nm, limited by the small thickness of the ITO film. Such low retardance is not enough for phase or polarization shaping but can be used for multiplexed optical data storage.

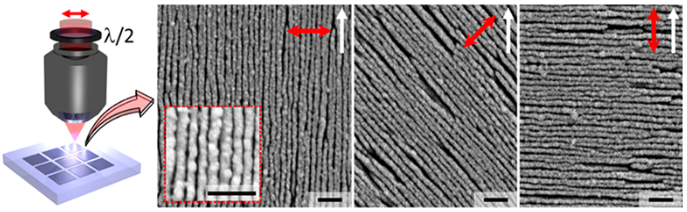

Fig. 11. SEM images of femtosecond laser nanostructured ITO film. The orientation (red arrows) of the linearly polarized laser beam was controlled by a half-wave plate (λ/2) placed before the objective. White arrows indicate the scanning direction. Processing conditions: 1030 nm wavelength, 400 fs pulse duration, 680 nJ pulse energy, focusing via 0.03 NA lens, 1 mm/s scanning speed, 500 kHz repetition rate. Scale bar is 500 nm. Reproduced from [28] under CC BY 4.0.

In order to obtain higher retardance, we can induce nanoripples on a thin film with a higher refractive index and larger thickness. For example, when nanoripples were generated on a 300 nm amorphous silicon film, the highest retardance was 0.55 π at a wavelength of 546 nm (Fig. 12). At pulse densities higher than 10^5 pulses/mm, nanogratings with a period of about 300 nm ($\lambda_{laser}/3$) were observed, which were perpendicular to the laser beam polarization. The retardance drops dramatically for pulse densities larger than 10^6 pulse/mm since nanogratings are replaced by nonbirefringent ripples with the period of λ_{laser} and orientation parallel to laser beam polarization direction. Considering the retardance of 0.55 π at a wavelength of 546 nm, 150 nm and the 300 nm thickness of the film, the estimated form birefringence is $\Delta n = n_e - n_o \approx -0.5$, which is two orders of magnitudes higher than that commonly observed in uniaxial crystals, such as quartz, sapphire or femtosecond laser nanostructured silica glass. Some thin optical elements were fabricated based on nanoripples induced on a-Si film and will be presented in section 4. Moreover, after femtosecond laser irradiation, large area nanoripples with associated form birefringence of -0.18 can be induced on a graphene oxide film and corresponding polarization-dependent devices were demonstrated [101].

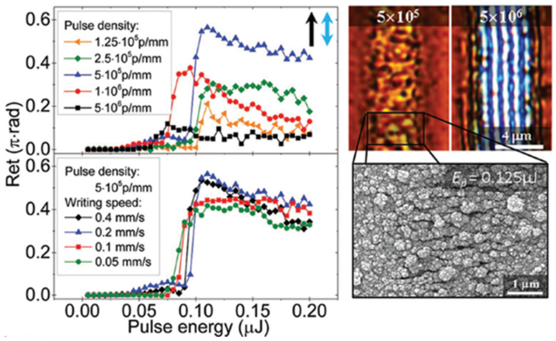

Fig. 12. Femtosecond laser-induced periodic a-Si:H film structures. Retardance dependence on pulse energy for different pulse densities (left top graph) and writing speeds (left bottom graph). On the right, optical and SEM images of periodic structures induced under 5×10^5 pulses mm^{-1} (left, subwavelength birefringent structure) and 5×10^6 pulses mm^{-1} (right, wavelength-size nonbirefringent ripples). Processing conditions: 1030 nm wavelength, 360 fs pulse duration, 125 nJ pulse energy, focusing via 0.03 NA lens, 100 kHz repetition rate. Reproduced from [29] under CC BY 4.0.

3.5. Periodic crystallization in glass

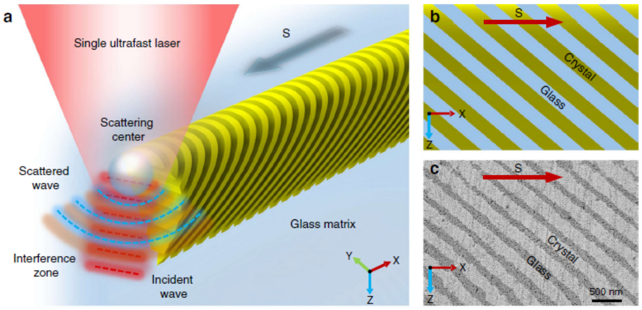

Fig. 13. Writing of periodic crystallization in the LTN glass. (a) Schematic diagram of the photonics texture formation by the interference field by scanning of a single laser beam in the glass. (b) and (c) Schematic diagram and high-resolution SEM image of the photonic textures. The arrows represent the beam scanning direction (denoted by S). Reproduced from [109] under CC BY 4.0.

Ultrafast laser direct writing is not only able to produce different nanostructures in transparent materials, but also can induce phase transition from crystalline to amorphous or vice versa, which has been used for 3D nonlinear photonics crystals [102–104] and fabrication of perovskite quantum dots in glass [105]. For example, nanocrystallization has been reported in lithium niobium silicate glasses (Li_2O-Nb_2O_3-SiO_2, LNS glass) by femtosecond laser writing [106]. Different crystallization regimes in the LNS glass can be classified by the increase of laser fluence and quasi-periodic distribution of nanocrystals was observed perpendicular to the polarization direction of laser writing beam [107]. More recently, continuous periodic crystallization was demonstrated in La_2O_3–Ta_2O_5–Nb_2O_5 glass (LTN glass) by ultrafast laser writing on laser-prepared crystallite seeds [108]. Such modifications have been used for data storage by rewriting the crystallization region with different polarization directions of the laser beam. In addition, 3D interference field in the LTN glass excited by ultrafast laser pulses has been utilized to generate highly regular periodic crystalline photonic textures (Fig. 13(a), b) [109]. The high-resolution

SEM image reveals clear periodic crystal and glass distribution (Fig. 13(c)), in which the period can be controlled by the focused depth and pulse energy. The reported approach is generic for different transparent materials from glasses to crystals, such as fused silica, quartz and sapphire [109], indicating it is a general principle for the fabrication of all-inorganic photonics.

3.6. Anisotropic modifications and applications

We reviewed different types of anisotropic modifications by ultrafast laser writing in transparent materials and will present their applications in next two sections: beam shaping (Section 4) and multiplexed optical data storage (Section 5). Before going into more details, we summarized each of them is suitable for what kind of applications (Table 1). Smooth nanogratings (type II smooth) and ultra-low loss anisotropic nanopores (type X) can be produced in silica glass and they are suitable for geometric phase and polarization shaping as well as optical data storage. The single nanolamella-like structures in silica glass are ideal for optical data storage but cannot be used in beam shaping elements due to their low retardance levels. On the other hand, nanoripples induced on thin films can be used for the fabrication of optical elements and single layer optical data storage, limited by the thickness of hundreds of nm. The recently reported periodic crystallization in the LTN glass by ultrafast laser writing has been used for the demonstration of data storage.

Table 1. Anisotropic modifications and their suitable applications.

	Class name	Material	Beam shaping	Optical data storage
Smooth nanogratings	Type II smooth	Silica glass	Yes	Yes
Oblate nanopores	Type X	Silica glass	Yes	Yes
Single nanolamella	Type S	Silica glass	No	Yes
Nanoripples	HSFL	Thin film	Yes	Single layer
Periodic crystallization		LTN glass	No	Yes

4. Geometric phase and polarization shaping elements

Recently, flat optics based on geometric phase (GP) has emerged as a promising type of optics to replace the bulky conventional optical elements based on the optical phase difference [45,110]. For example, we can achieve any phase change by controlling the azimuth of the slow axis, $A(x, y)$, of locally imprinted nanostructures. When the retardance is half-wave and the incident light is circularly polarized, the relative phase change is equal to $\varphi(x, y) = \pm 2A(x, y)$, where the sign is defined by the handedness of the input light. Therefore, different phase elements, including lenses, gratings and hologram patterns, can be realized by manipulation of laser-induced nanostructures [111,112].

On the other hand, polarization converters can be designed for linearly or circularly polarized incident beams. For instance, a half-wave plate with locally varying slow axis orientations can be constructed to produce a radial distribution of the electric field for an incident beam with linear polarization. For the circularly polarized incident beam, a radial or azimuthal polarization can be generated with a space variant quarter-wave plate with radial symmetry. In this section, we discuss both spatial variant phase and polarization shaping elements based on ultrashort laser-induced nanostructures in thin film and silica glass.

4.1. Elements based on nanostructured amorphous silicon film

As mentioned before, nanoripples can be created on an amorphous silicon film by femtosecond laser writing. One geometric phase diffraction grating with a period of 30 µm was fabricated on the a-Si film, where the geometric phase changing in the x-direction (Fig. 14(a)). However, the retardance is around 0.4 π at a wavelength of 532 nm and a part of transmitted light is projected to the 0th order as a nondiffracting beam (Fig. 14(b)). Also, the handedness of the diffracted circularly polarized beam is flipped, which is a signature of geometric phase elements. The low efficiency of around 36% can be improved by polarization filtering to eliminate the 0th order beam or by introducing retardance of half-wave, which can be realized with a thicker a-Si film.

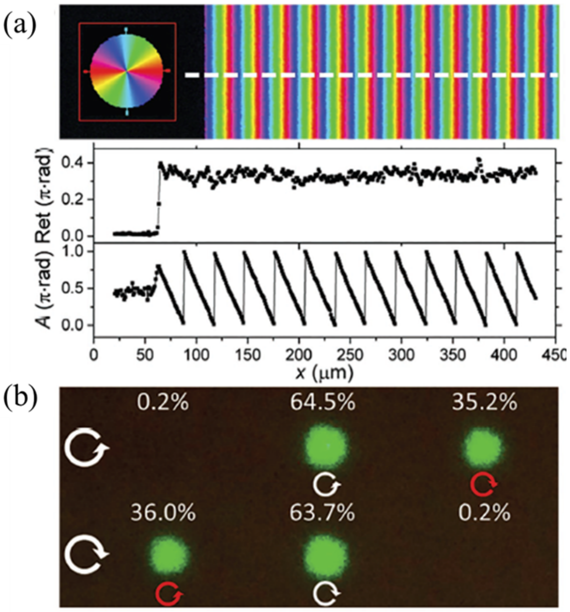

Fig. 14. Femtosecond laser direct writing of GPOE designed as a polarization grating (PG). (a) Imprinted PG with a period of 30 μm: birefringence image and profile of retardance and slow axis extracted from the top image. Pseudo colors (inset) indicate the local orientation of slow axis. (b) Laser beam profiles with a wavelength of 532 nm for right-handed circular (top) and left-handed circular (bottom) polarizations, and their corresponding diffraction efficiencies and polarization states (white and red circular arrows) produced by PG. Reproduced from [29] under CC BY 4.0.

In addition, a 1 mm polarization and phase converter with azimuthal phase distribution (Fig. 15(a)) was fabricated to generate optical vortices with radial or azimuthal polarization. The topological charge of the element was -1, resulting in the orbital angular momentum with the opposite sign compared to the input spin momentum. The average retardance of the element was ~0.5 π at 532 nm, which served as a quarter-wave plate. To verify the radial/azimuthal polarization optical vortex, the converter was characterized by a left/right-handed circularly polarized continuous wave (CW) laser beam with a wavelength of 532 nm. The laser beam was simulated using the algorithm based on the Jones matrix and Fourier propagation. After a linear polarizer, the typical propeller-shaped interference was observed (Fig. 15(e)-(j)), indicating the success of the imprinted radially symmetric GPOE.

The other example of GPOE is a computer-generated geometric phase Fourier hologram (CGH), which converts the incident Gaussian beam into designed intensity distribution. After the circularly polarized incident beam passed through the CGH element, the target image was reconstructed by the Fourier transformation property of a positive lens (Fig. 16(a)). The adapted weighted Gerchberg-Saxton algorithm was used to encode the “Light” logo with an eight-bit grayscale CGH element (Fig. 16(b), c). The geometric phase is independent of wavelength, so the phase profile for different wavelengths should be the same (Fig. 16(d)). The intensity patterns

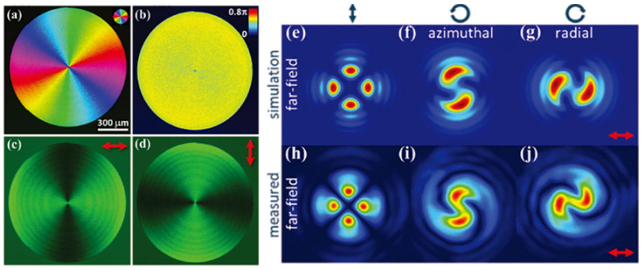

Fig. 15. Radial and azimuthal polarization optical vortex converter for circular incident polarization. (a) azimuth of slow axis orientation and (b) averaged retardance value of roughly 0.5π specifies GPOE as a quarter-wave plate at wavelength of 532 nm. Pseudo colors indicate the direction of slow axis. Color bar: 0–0.8π rad. (c) and (d) Linearly polarized optical transmission images of polarization sensitive element illuminated by circularly polarized light. Reproduced from [29] under CC BY 4.0.

are different for wavelengths because each wavelength is diffracted to a different angle due to the different wave vectors (Fig. 16(e)-(f)).

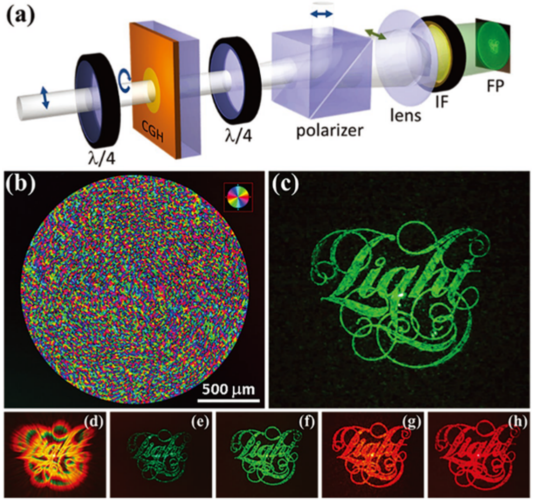

Fig. 16. Computer-generated geometric phase Fourier hologram (CGH). (a) Setup for target image reconstruction: quarter-wave plates (λ/4), laser imprinted eight-bit grayscale CGH, linear polarizer, lens with f = 50 mm, interference filter (IF), Fourier plane (FP). Blue arrows indicate the state of beam polarization. (b) Birefringence image of laser-imprinted CGH and (c)–(h) reconstructed image. The hologram was illuminated with (c) 532 nm laser beam and (d)–(h) supercontinuum laser beam, where (d) 450–950 nm, (e) 500 nm, (f) 550 nm, (g) 600 nm, and (h) 650 nm filtered wavelengths. Reproduced from [29] under CC BY 4.0.

The applications of nanostructured a-Si film were demonstrated as geometric phase elements and could be applied to any materials that support the formation of nanoripples including semiconductors and dielectrics. Although the thin film can be integrated into flat optics, the relatively low efficiency and retardance prevent its practical applications.

4.2. Elements based on smooth nanogratings in silica glass

Different from thin films, the longitudinal length of volume nanogratings can be much larger in silica glass, especially when writing multilayer nanogratings. Therefore, the retardance can be as large as π or 2π for visible light, which is ideal for both geometric phase elements and polarization converters. As a demonstration, a polarization grating (PG) with geometric phase varying in the x-direction was imprinted in silica glass based on smooth nanogratings (Fig. 17(a)) and the transmission of which was 90%. The period of the PG was 60 µm and the average retardance was ∼ π at a wavelength of 532 nm (Fig. 17(b)). The 90% of the transmitted light was diffracted to ±1st order depending on the handedness of the incident circularly polarized light and 10% was projected to the 0th and higher orders (Fig. 17(c), d).

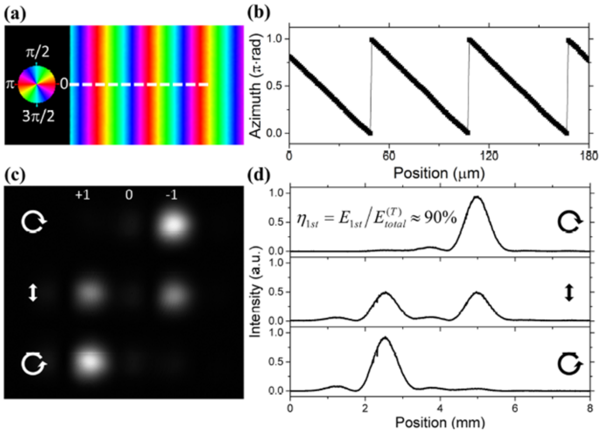

Fig. 17. Femtosecond laser direct writing of GPOE designed as a polarization grating (PG) with a period of 60 µm. (a) Birefringence image of the imprinted nanogratings; (b) the profile [white dashed line in (a)] of the azimuth of the slow axis extracted from the birefringence image. Pseudo colours (inset) indicate the local orientation of the slow axis. (c) 532 nm laser beam profiles of the transmitted right-handed circular (top), linear (middle), and left-handed circular (bottom) polarizations, and (d) its corresponding intensity profiles with the estimated first order diffraction efficiency. White and black arrows indicate the polarization state of the incident and PG transmitted beams. Reproduced from [65] under CC BY 4.0.

In addition, a geometric phase element with 8-bit grayscale CGH was designed for Queen Elizabeth portrait II with a pixel spacing of 1.2 µm (Fig. 18(a), b). The half-wave retardance was ensured in this element to obtain high efficiency. The reconstructed image was captured after a positive lens and within the spectral range of 450–950 nm (Fig. 18(c)-(f)). The key advantages of such smooth nanogratings based geometric phase elements are high durability and high efficiency of up to 90%. However, the degradation threshold and efficiency of elements based on recently found oblate nanopores are even better.

4.3. Elements based on ultralow loss oblate nanopores

The ultralow-loss birefringent modification consisting of oblate nanopores provides a variety of birefringent optical elements, such as GPOEs, vector beam converters, and true zero-order waveplates. A GP prism or polarization grating has been fabricated, where the slow axis orientation varies along the x-direction (Fig. 19(a)). The average retardance was around 220 nm, which is close to π at the wavelength of 457 nm. The demonstrated diffraction efficiency was higher than 99% at 457 nm and the diffraction direction can be switched by selecting the left/right hand circularly polarized incident beam. A GP lens with a parabolic shape was fabricated as well

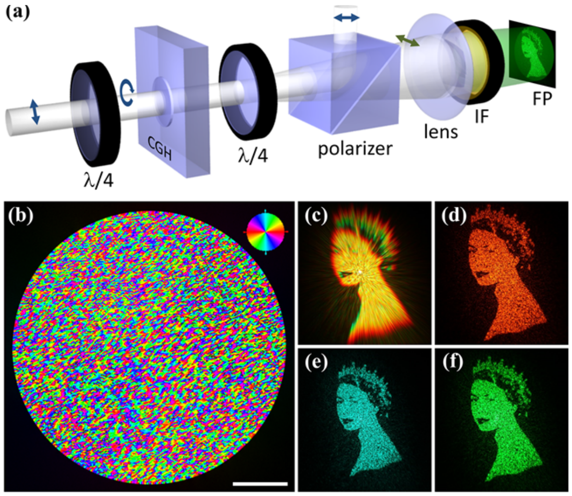

Fig. 18. Computer generated geometric-phase Fourier hologram. (a) Setup for polarization filtering and target image reconstruction: quarter-wave plates (λ/4), laser imprinted 8-bit grayscale CGH, linear polarizer, lens with f = 50 mm, interference filter (IF), Fourier plane (FP). Arrows indicate the state of beam polarization. (b) Birefringence image of laser-imprinted CGH, and (c)–(f) its resulting reconstructed images. Pseudo colours (inset) indicate the local orientation of the slow-axis. The hologram was illuminated with a supercontinuum laser beam with (c) 450-950 nm, (d) 600 nm, (e) 500 nm, and (f) 550 nm filtered wavelengths. Scale bar is 500 µm. Reproduced from [65] under CC BY 4.0.

(Fig. 19(b)). The focusing and defocusing can be realized by changing the handedness of the circular polarization. The focused beam size is 112 µm, which is close to the theoretical value of 114 µm. Interestingly, the same highly transparent GP lens in glass could act as an all-in-one concave-convex lens for the correction of short and long-sightedness.

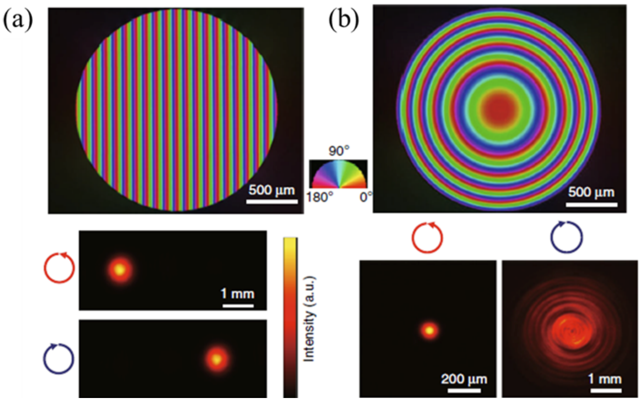

Fig. 19. Geometric phase (GP) optical elements imprinted with the low-loss birefringent modification. (a) Birefringence image of a GP polarization grating with a slow axis gradient of 0.01 π rad μm^{-1} (upper), and light intensity patterns of 457 nm CW laser beams with different circular polarizations diffracted by the GP prism (lower). (b) Birefringence image of a GP lens, and intensity patterns of 488 nm CW laser beams with different circular polarizations focused and defocused by the GP lens. The focal lengths are ±208mm for the wavelength of 488 nm. Reproduced from [66] under CC BY 4.0.

Moreover, a 10 mm polarization vector beam converter was fabricated for the wavelength of 343 nm (Fig. 20(a)). The converter is highly transparent, while it could be clearly observed under cross-polarizers. The average retardance was ~170 nm, which was 0.5 π of the target wavelength and the slow axis azimuth was half of the polar angle. A high-quality 343 nm donut-shaped beam with radial or azimuthal polarization was generated (Fig. 20(b)). Transmittance through the beam converter as high as 91% was measured without any evidence of damage for the 343 nm laser beam with an average power of 1.2W, beam width of 4mm, pulse duration of 190 fs and repetition rate of 1MHz. For pulse duration of 300 fs, the measured degradation threshold of type X modification was 7 TW/cm^2, which is higher than the value of 5.2 TW/cm^2 for type II modification [113], indicating that elements based on type X modification are suitable for high power laser applications. Moreover, a modal vortex beam was generated by an ultralow loss beam shaper and the propagation properties were characterized [114]. An ultralow loss spatially variant waveplate was used to directly generate a radially polarized beam from an Nd: YVO$_4$ laser using a ring-shaped pump beam [115].

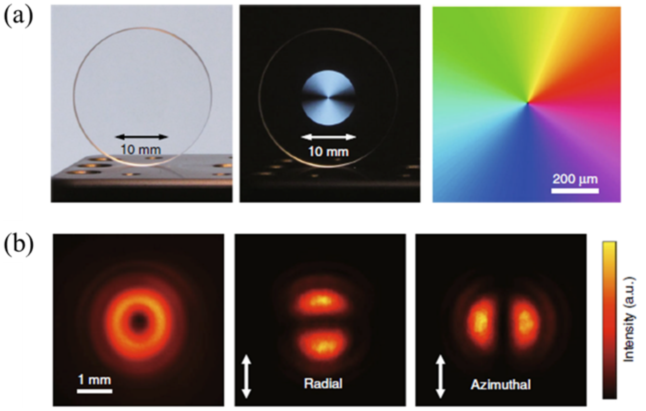

Fig. 20. Vector beam converter imprinted with the low-loss birefringent modification. (a) 10 mm vector beam converter without (left) and with (middle) a polarizer under linearly polarized white light illumination. The slow axis distribution in the central part of the converter is shown on the right. (b) Intensity pattern of a 343 nm laser beam after the converter without a polarizer (left). Intensity patterns of the radial (middle) and azimuthal (right) vector beams produced by the converter after a polarizer. Reproduced from [66] under CC BY 4.0.

4.4. Comparison of birefringent modifications for beam shaping

Since different anisotropic nanostructures have been used for geometric phase and polarization shaping element, it is necessary to compare their core features and fabrication conditions (Table 2). For nanoripples induced on thin films, the birefringence is as high as -0.5 but the low retardance of around 130 nm (0.4 π at the wavelength of 532 nm) limited by the thickness of film and low conversion efficiency of 64% prevent their practical applications. The birefringence of smooth nanogratings based modification is -0.004 and the longitudinal length is 60 µm, leading to the retardance of π for a single layer modification. In contrast, the birefringence of type X (-0.0008) structures is one order of magnitude lower than that of type II smooth, so six layers of ultralow loss birefringent modification were written to achieve the same retardance level. The conversion efficiency of elements depends on the transmission of the modifications, so the type X modification has the highest efficiency (>99%). The repetition rates of writing laser pulses used for different modifications are listed here as well. The optimal repetition rate for type II smooth and type X elements fabrication is 200 kHz since unwanted damage happens at higher repetition rate for line writing. However, the highest repetition rate for writing of type X dots is 2 MHz and the further comparison and explanation will be reported elsewhere.

Table 2. Comparison of different modifications for beam shaping elements.

	Birefringence $\cdot n_b$	Retardance at 532 nm	Efficiency (%)	Layer number	R.R. (kHz)
Nanoripples	-0.5	0.4 π	~64	1	500
Smooth nanogratings	-0.004	π	~90	1	200
Oblate nanopores	-0.0008	π	>99	6	200

5. 5D optical data storage

Since the first demonstration of 5D optical data storage in silica glass by femtosecond laser writing, how to improve the writing speed and data capacity is an evergreen challenge for researchers. The data writing speed is limited by several factors, such as modulation frequency for the polarization control unit and the number of pulses for each data voxel. An electro-optic modulator (EOM), a Pockel cell, with a modulation rate of ~MHz was used to replace the liquid crystal spatial light modulator with a refresh rate of 60 Hz. In addition, the number of pulses for each voxel was reduced to 20 for flattened nanopores or less than 10 for single nanolamella structures. Therefore, the data writing speed was improved from several B/s up to MB/s. In order to increase data capacity, both the lateral voxel separation and layer separation should be reduced. Here, we review the recent progress of 5D optical data storage based on oblate nanopores (type X) and single nanolamella-like structures (type S).

5.1. Type X based data storage

The significant advantage of oblate nanopores is their ultrahigh transmission, which is larger than 99% in the visible range. The ultrahigh transmission allows recording and retrieving thousands of layers of multibit digital data practically. To reach a high data capacity, data bits per voxel is a crucial factor, determined by the number of retardance and azimuth levels. For the data writing demonstration, we firstly investigated the laser parameters for type X data voxels. The repetition rate was 500 kHz, the pulse duration was 300 fs, and the NA of the aspheric lens was 0.16. When the pulse energy was higher than 900 nJ or a number of pulses larger than 500 for pulse energy from 450 to 800 nJ, only nanogratings based type II modification was observed. The ultralow-loss type X modification was generated for a number of pulses from 40 to 300 at a pulse energy of 550 nJ, which is invisible in an optical image (Fig. 21(a), b). It is noticeable that the retardance error of type II was larger than that of type X (Fig. 21(c)) due to larger fluctuations of aspect ratios of elongated nanostructures. Since the retardance of type X modification can be as high as 18 nm, multiple retardance levels were realized by different numbers of writing pulses. In addition, the azimuth and retardance error (≈0.9° and ≈0.5 nm) were comparatively low (Fig. 21(d)). Four distinguishable retardance levels and 32 azimuths were used to encode 7-bit information to one voxel with a nearly 100% readout accuracy (Fig. 21(e)). Although the data capacity is improved by 75% compared with 4-bit per voxel, the drawback is a relatively low writing speed of ≈0.2 kB/s.

Despite 7 bits per voxel was achieved, a large lateral voxel separation of 5 μm is necessary to obtain 100% accuracy by eliminating the crosstalk between voxels with a large modification size. A lens with a higher NA of 0.3 was utilized to write voxels with a smaller size and then reduce the lateral voxel separation and layer separation to 2 and 17.5 μm, respectively. The writing of 4-bit data per voxel with a scanning speed of 30mm/s leads to ≈9 times higher data capacity and ≈43 times higher recording speed.

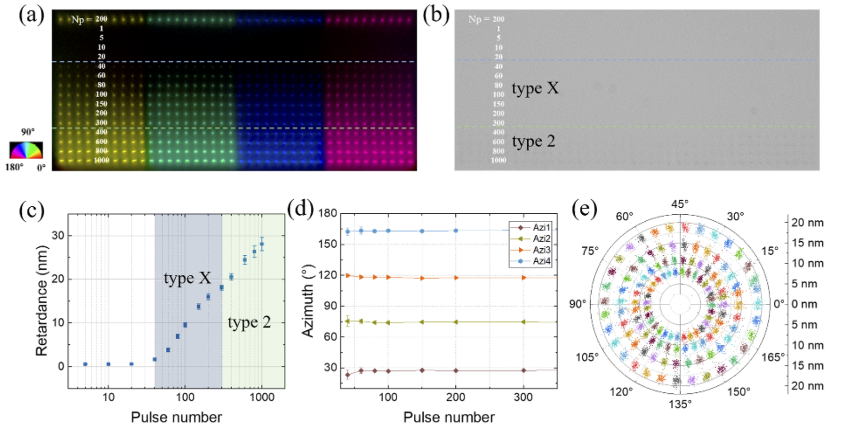

Fig. 21. Experimental demonstration of 7 bits per voxel in silica glass. (a) The birefringence image of voxels imprinted by four polarizations and different pulse numbers at energy of 550 nJ. (b) Corresponding optical transmission image of (a). (c) The measured retardance dependence on pulse number from (a). The transition from type X to type II occurs at $N_p = 400$. (d) Azimuth for the four different slow axes in (a). (e) Polar diagram of the 4 levels retardance and 32 levels azimuth. The 4-level retardance corresponds to $N_p = 80$, 100, 140, and 250. Lateral voxel separation is 5 μm. Reproduced from [67] under CC BY 4.0.

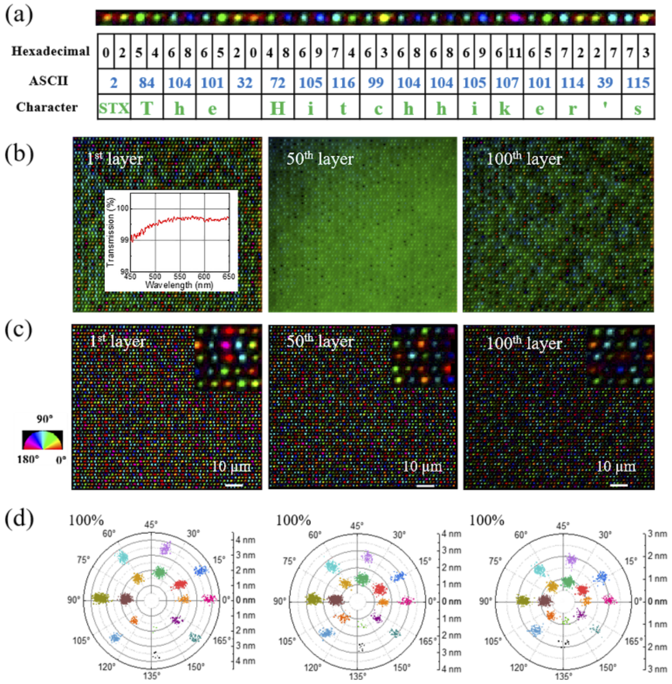

Hexadecimal	0	2	5	4	6	8	6	5	2	0	4	8	6	9	7	4	6	3	6	8	6	8	6	9	6	11	6	5	7	2	2	7	7	3
ASCII	2		84		104		101		32		72		105		116		99		104		104		105		107		101		114		39		115	
Character	STX		T		h		e				H		i		t		c		h		h		i		k		e		r		'		s	

Fig. 22. 100-layer 5D optical data storage by ultralow-loss oblate nanopores. (a) Illustration of data encoding and decoding. (b) The birefringent images of data voxels of different layers. Inset is the transmission of 100-layer data in the visible range. (c) The birefringent images after removing the background of (b). Insets are enlargements of small region (10 μm × 10 μm). (d) Polar diagram of the measured retardance and azimuth of all voxels in (c). Reproduced from [67] under CC BY 4.0.

For a demonstration of ultralow-loss data writing, an iconic book was written in 100 layers with transmission higher than 99% in the visible range (Fig. 22). Eight azimuths and two retardance (N_p=20 and 30) levels were used to achieve 4 bits ($2^3 \times 2^1$) of information per voxel. The text data were encoded by American Standard Code for Information Interchange (ASCII) code and written from the bottom layer (the 100th layer, 1878 μm beneath the top surface) to the top layer (the first layer, 146 μm beneath the top surface). To retrieve the text, the 2 retardance and 8 azimuth levels of each spot were normalized and discretized after being extracted from raw data, so the hexadecimal number was equal to Ret. + 2 × Azi. (Ret. = 0, 1; Azi. = 0, 1, . . . , 7) can be calculated, every two of voxels correspond to a character (Fig. 22(a)). However, the readout accuracy of recorded data was as low as ~80%, which can be attributed to the strong background caused by the birefringence of surrounding layers (Fig. 22(b)). In order to achieve higher accuracy, the strong background was removed by an algorithm to acquire the background-free images with precise retardance and azimuth of each voxel (Fig. 22(c)), resulting in 100% readout accuracy for all the 1st layer, the 50th layer, and the 100th layer (Fig. 22(d)).

As the lateral size of voxels increases with the writing pulse number, the lateral voxel separation can be reduced from 2 µm to 1.5 µm using one retardance level produced by 20 pulses, improving the data recording speed to 25 kB/s. Data recording was demonstrated at a repetition rate of 1 MHz, which is the maximum of the Pharos laser. But type X was also observed in a preliminary experiment with a repetition rate of 2 MHz by Satsuma laser, implying twice the data writing speed can be obtained.

5.2. Type S based data storage

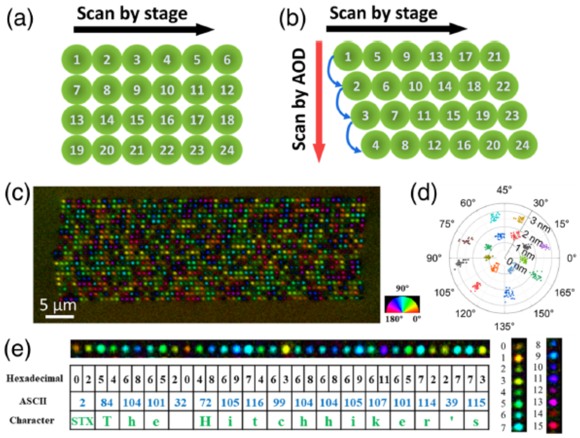

Hexadecimal	0 2	5 4	6 8	6 5	2 0	4 8	6 9	7 4	6 3	6 8	6 8	6 9	6 11	6 5	7 2	2 7	7 3
ASCII	2	84	104	101	32	72	105	116	99	104	104	105	107	101	114	39	115
Character	STX	T	h	e		H	i	t	c	h	h	i	k	e	r	'	s

Fig. 23. Optical data storage of 5 GB data. (a) Schematic diagram of raster scanning by stage translation and (b) combination of raster and AOD scanning. Each green circle indicates one data voxel, and the numbers show the temporal sequence of data recording. (c) Birefringent voxels written by the PEM method with 10-channel AOD. The pulse trains include one seeding pulse and seven (or four) writing pulses (515 nm, 250 fs, 10 MHz, 96 mm/s, 9.6×10^5 voxels/s). Pseudo-colors (inset) indicate the local orientation of the slow axis. (d) Polar diagram of eight azimuths of slow axis orientation and two levels of retardance from (c). (e) Illustration of data encoding and decoding. Reproduced from [68] under CC BY 4.0.

Although type X modification was used for 100-layer 5D optical data storage, the data writing speed is just ~10 kB/s, limited by laser repetition rate and the number of pulses for each voxel. Alternatively, single nanolamella structures (type S) written by a few pulses at a 10 MHz repetition rate can be used to improve the speed of data writing. A 10 MHz laser with a wavelength of

515 nm was utilized to write birefringent voxels with a rate of 10^6 voxels/s by five or eight pulses. However, such high throughput by raster scanning with the lateral voxel separation of 1 µm requires a translation velocity as high as 1000 mm/s (Fig. 23(a)), which is difficult to be implemented precisely. As a more pragmatic solution, we used an acousto-optic deflector (AOD) in the optical setup to scan the focused laser spot in the direction perpendicular to the stage scanning direction (Fig. 23(b)). For the number of AOD channels chosen as 10, the stage translation speed could be reduced to 100 mm/s for 10^6 voxels/s writing (Fig. 23(c)). The 4-bit data readout accuracy for a single layer without any error correction algorithm was 100% (Fig. 23(d)), suggesting this method can be utilized for practical 5D data storage.

The amount of 5 GB digital data was written in 120mm × 2.4mm across 50 layers in the bottom-to-top order with the parameters of dot separation 1.2 µm, layer separation 10 µm, stage scanning speed 90 mm/s, and AOD channel number 8, leading to the actual data writing speed of 225 kB/s and the imprinting rate of 6×10^5 voxels/s. The text data were encoded by the ASCII code, where every two voxels correspond to a character and the hexadecimal number of each spot varies from 0 to 15 (Fig. 23(e)). The data readout accuracy for both the top and bottom layers is close to 100%. Applying the same parameters, 1.64 TB of digital data can be stored in a silica glass plate of 127 mm in size and 3mm in thickness.

5.3. Comparison of type X and type S based data storage

Multiplexed optical data storage based on oblate nanopores (type X) or single nanolamella structures (type S) has shown great potential for practical application and it is necessary to compare their advantages and disadvantages.

The data writing speed is limited by lateral voxel separation (Δx), stage scanning speed (V_s) and the number of bytes per voxel (N_b). The channel number (N_c) is 10 for type S writing and is 1 for type X writing, meaning no AOD is used for the writing of type X. Therefore, the data writing speed (V_w) can be calculated as:

$$V_w = \frac{V_s}{\cdot x} \times N_b \times \mathrm{N}_c \tag{3}$$

The data writing speed for type X and type S is 11 kB/s and 500 kB/s, respectively (Table 3). Not only the ratio between scanning speed and lateral voxel separation limits the data writing speed, but also the ratio between laser repetition rate and a number of pulses for each voxel. The writing of type S structures by a 10 MHz laser requires less than 8 pulses, while the maximum repetition rate for type X formation is around 2 MHz (limited with heat accumulation) and 20 pulses are necessary to imprint one voxel.

Table 3. Comparison of data writing speed between type X and type S.

	Δx (µm)	V_s (mm/s)	N_b (B/voxel)	N_c	V_w (kB/s)
Type X	2	45	0.5	1	11
Type S	1	100	0.5	10	500

Another important parameter is the data capacity per silica glass disk, which is 127 mm long and wide and 3 mm thick. Considering lateral voxel separation (Δx) and layer separation (Δz), we can calculate the maximum voxel number in the disc. The number of bytes per voxel is 0.5 for both cases, so the data capacity can be calculated as:

$$Capacity = \frac{d^2 t}{\cdot x^2 \cdot z} \times N_b \tag{4}$$

The current data capacity of a silica plate by type X and type S voxels is 250 GB and 2.42 TB, respectively (Table 4). The potential data capacity of a fuse silica disc could be 20 TB for type X [67] and 500 TB for type S [68] with further efforts.

Table 4. Comparison of data capacity between type X and type S.

	·x (μm)	·z (μm)	N_b (Byte/voxel)	d (mm)	t (mm)	Capacity (GB/disk)
Type X	2	17.5	0.5	127	3	350
Type S	1	10	0.5	127	3	2420

Although the 5D data storage based on type S modification has higher writing speed and capacity, the disadvantage is the transmission of multilayer data voxels is lower than that for type X. For instance, the transmission for 20 layers of single nanolamella structures is 90%, compared to 99% for type X modification. If the number of layers increases, stronger interlayer crosstalk makes the readout accuracy lower than 100%, which is not a problem for type X data storage. Therefore, the recording and retrieving thousands of layers of type X data voxels could be a potential option for practical optical data storage in the future.

5.4. Other ways to improve optical storage

Besides the already mentioned single nanolamella-like structures (type S), there are other ways to increase the writing speed of optical data storage. One example is writing birefringent modifications with a small number of laser shots at a burst mode. The second harmonic (515 nm) was used with a repetition rate of 1 MHz and a pulse duration of 190 fs. In the burst mode, each pulse group contains 7 pulses with a time interval of 15.4 ns, instead of single pulses in the standard mode (Fig. 24(a)). Distinguishable birefringent voxels can be written by only 10 shots of bursts, while birefringent dots imprinted by 10 pulses in the standard mode cannot be used in data storage due to their low retardance and azimuth accuracy (Fig. 24(b), c). Considering 10 shots for one voxel and 1 MHz repetition rate, the maximum voxel writing rate is 10^5 voxels/s with burst writing. In addition, the retardance of data voxels written by 40 shots of burst is higher than 40 pulses without burst, indicating burst writing can improve retardance as well.

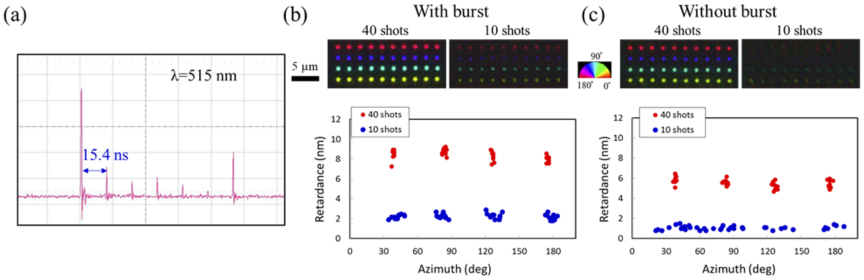

Fig. 24. Birefringent voxels written with the burst mode. (a) Temporal profile of femtosecond laser burst measured by a digital oscilloscope. The number of pulses is 7 and the time interval is 15.4 ns. Birefringent voxels writing with (b) and without (c) burst mode. The total energy of one shot in (b) was 55 nJ and the single pulse energy in (c) was 30 nJ. Processing conditions: 515 nm wavelength, 190 fs pulse duration, focusing via 0.55 NA lens, 1 MHz repetition rate.

In order to further increase writing speed, parallel seeding and writing was proposed to imprint one voxel with only one shot of burst. A circularly polarized seeding beam with 5 spots generated by a SLM and a linearly polarized writing beam were combined by a non-polarizing beam splitter and focused via a 0.55 NA aspheric lens in silica glass (Fig. 25(a)). The silica glass was firstly irradiated by multi-spot seeding beam and then the writing beam was focused on the position where has been seeded by 10 shots of burst. Because multiple seeding and writing processes are performed in parallel, the seeding time is negligible, and the writing speed is significantly improved. Birefringent voxels with high quality can be imprinted by only one or two shots of burst from writing beam, implying the maximum output is 5-10 × 10^5 voxels/s with a 1 MHz repetition rate (Fig. 25(b)). However, how to achieve 4 bits per voxel for practical optical data storage with 100% readout accuracy requires further study.

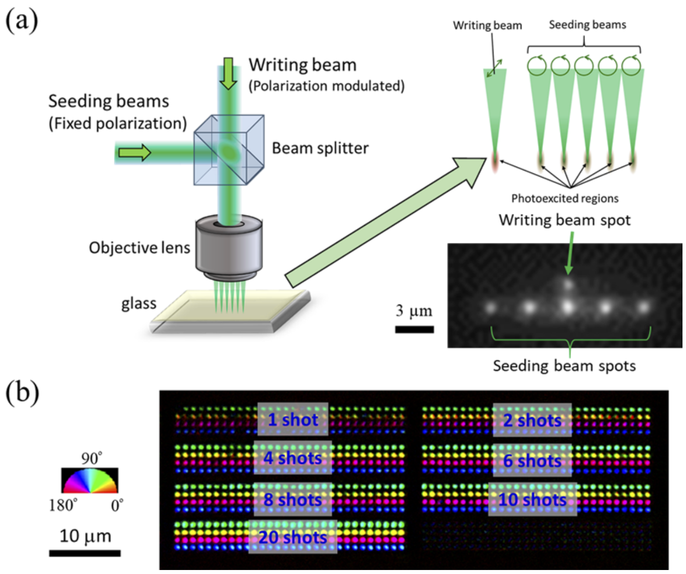

Fig. 25. Parallel seeding-writing method with the burst mode. (a) Illustration of a circularly polarized seeding beam with five spots and a single linearly polarized writing beam. (b) Birefringence image of voxels written by parallel seeding-writing method. The seeding shot number is fixed to 10 and the writing shot number varies from 1 to 20. Processing conditions: 515 nm wavelength, 64 (59) nJ seeding (writing) burst energy; 190 fs pulse duration, focusing via 0.55 NA lens, 1 MHz repetition rate, 1 μm voxel separation.

Similar seeding and writing method can also be used to improve the writing speed of type X voxels. For the seeding part, circularly polarized pulses (1030 nm, 300 fs) were focused via a 0.16 NA lens in silica glass to create a region with isotropic nanopores, in which no detectable birefringence was measured. Hereafter, birefringent voxels were written in this pretreated region using different numbers of linearly polarized pulses. An ultralow loss birefringent voxel with ~2 nm retardance was written by only a single pulse and the slow axis orientation was perpendicular to the polarization direction of the laser beam (Fig. 26), implying higher writing speed is possible for type X based data storage by pretreatment. Besides, higher retardance can be realized by increasing the number of writing pulses, enabling multiple retardance levels for storage application. The writing of type X voxel by a few pulses in a pretreated region is based on near-field enhancement, which is not dependent on writing pulse duration.

A nanoporous glass (NPG) sample with $98SiO_2$•$1.6B_2O_3$ • $0.4Na_2O$ chemical composition and average pore size from 5-10 nm was prepared to reduce the writing pulse number without seeding by laser pulses [116]. A burst of laser pulses with a time interval of 98 ns was generated by a homemade resonator. Optical data storage with 3 bits of information per birefringent voxel and 100% readout accuracy can be realized by a single shot of burst with a 10 kHz repetition rate in the NPG sample [117]. More recently, the same research group demonstrated that 3 pulses with a 1 MHz repetition rate can reshape nanostructures in the NPG sample to a single anisotropic cavity (Fig. 27) to improve the data writing speed for optical storage [118]. Nevertheless, the low optical transmission and small size of nanoporous glass limit its practical application in optical storage. On the other hand, to increase data capacity, a single nanoslit structure with

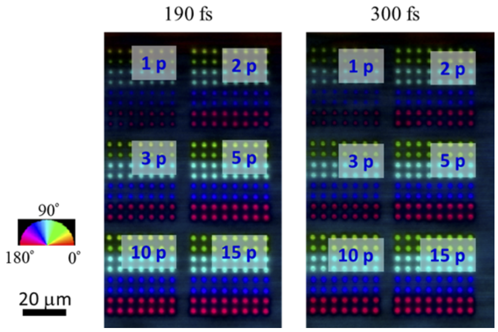

Fig. 26. Birefringence image of type X voxels written with different pulse numbers in a pretreated region. The pretreatment was carried out with circularly polarized pulses to create isotropic nanopores in silica glass. Processing conditions: 1030 nm wavelength, 700 nJ writing energy; 300/190 fs pulse duration, focusing via 0.16 NA lens, 5 µm voxel separation.

width of ~40 nm can be created by hundreds of tightly focused laser pulses in fused silica [119]. Anisotropic nanostructures produced by two beams of femtosecond laser with a certain angle and a time delay of tens of picoseconds were imprinted for optical data storage, revealing more possibilities in anisotropic nanostructuring [120].

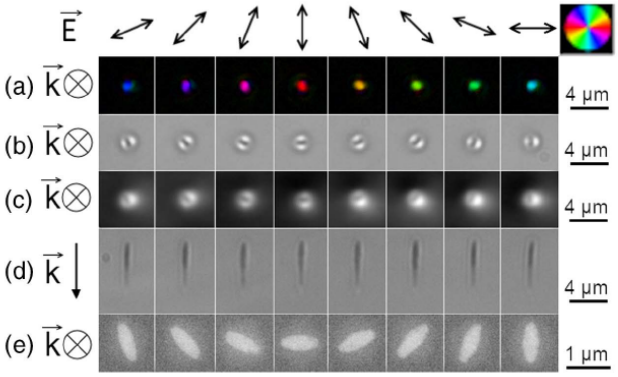

Fig. 27. Birefringent dots written by 3 ultrafast pulses in a nanoporous glass (NPG) sample. (a) Birefringence image, top view. (b) Bright-field image, top view. (c) Phase pattern of propagate light, top view. (d) Bright-field image, side view. (e) SEM images of the exposed dots, top view. Reproduced with permission from [118] © 2020 Optica Publishing.

6. Conclusion

In this review, we focused on recent progress in femtosecond laser anisotropic nanostructuring in transparent materials and its applications in beam shaping elements and multiplexed optical data storage. Although after femtosecond laser direct writing nanogratings in silica glass and nanoripples in thin films were used to construct phase and polarization shaping elements, nearly 100% efficiency was only achieved by ultralow-loss oblate nanopores (type X) in fused silica. On the other hand, highly localized single nanolamella-like structures (type S) by a few pulses were demonstrated to improve the writing speed and capacity of multiplexed optical data storage. More accurate and flexible control of pulse energy and polarization could enable advanced nanostructuring of various materials.

Funding. Microsoft (Project Silica); European Research Council (ENIGMA, 789116).

Acknowledgments. The authors are grateful to all our colleagues and collaborators contributed to the results review here: J. Qiu, A. G. Kazanskii, I. Abdulhalim, Y. Shimotsuma, M. Sakakura, L. Wang, Y. Yu, J. Zhang, R. Drevinskas, A. Cerkauskaite, A. Okhrimchuk, S. Fedotov, A. Lipatiev, S. Lotarev, I. Glebov, V. Sigaev and many others. We thank them all.

Disclosures. The authors declare no conflicts of interest.

Data availability. Data underlying the results presented in this paper are not publicly available at this time but may be obtained from the authors upon reasonable request.

References

1. A. Vogel, J. Noack, G. Hüttman, and G. Paltauf, "Mechanisms of femtosecond laser nanosurgery of cells and tissues," Appl. Phys. B **81**(8), 1015–1047 (2005).
2. S. Kawata, H.-B. Sun, T. Tanaka, and K. Takada, "Finer features for functional microdevices," Nature **412**(6848), 697–698 (2001).
3. S. Nolte, M. Will, J. Burghoff, and A. Tuennermann, "Femtosecond waveguide writing: a new avenue to three-dimensional integrated optics," Appl. Phys. A **77**(1), 109–111 (2003).
4. K. Sun, D. Tan, X. Fang, X. Xia, D. Lin, J. Song, Y. Lin, Z. Liu, M. Gu, Y. Yue, and J. Qiu, "Three-dimensional direct lithography of stable perovskite nanocrystals in glass," Science **375**(6578), 307–310 (2022).
5. A. Ródenas, M. Gu, G. Corrielli, P. Paiè, S. John, A. K. Kar, and R. Osellame, "Three-dimensional femtosecond laser nanolithography of crystals," Nat. Photonics **13**(2), 105–109 (2019).
6. A. Marcinkevičius, S. Juodkazis, M. Watanabe, M. Miwa, S. Matsuo, H. Misawa, and J. Nishii, "Femtosecond laser-assisted three-dimensional microfabrication in silica," Opt. Lett. **26**(5), 277 (2001).
7. Y. Bellouard, A. Said, M. Dugan, and P. Bado, "Fabrication of high-aspect ratio, micro-fluidic channels and tunnels using femtosecond laser pulses and chemical etching," Opt. Express **12**(10), 2120 (2004).
8. X. Zheng, B. Jia, H. Lin, L. Qiu, D. Li, and M. Gu, "Highly efficient and ultra-broadband graphene oxide ultrathin lenses with three-dimensional subwavelength focusing," Nat. Commun. **6**, 1 (2015).
9. H. Liu, W. Lin, and M. Hong, "Hybrid laser precision engineering of transparent hard materials: challenges, solutions and applications," Light: Sci. Appl. **10**(1), 1 (2021).
10. D. A. Parthenopoulos and P. M. Rentzepis, "Three-dimensional optical storage memory," Science **245**(4920), 843–845 (1989).
11. B. N. Chichkov, C. Momma, S. Nolte, F. Von Alvensleben, and A. Tünnermann, "Femtosecond, picosecond and nanosecond laser ablation of solids," Appl. Phys. A **63**(2), 109–115 (1996).
12. E. Glezer, M. Milosavljevic, L. Huang, R. Finlay, T.-H. Her, J. P. Callan, and E. Mazur, "Three-dimensional optical storage inside transparent materials," Opt. Lett. **21**(24), 2023 (1996).
13. Y. Shimotsuma, P. G. Kazansky, J. Qiu, and K. Hirao, "Self-organized nanogratings in glass irradiated by ultrashort light pulses," Phys. Rev. Lett. **91**(24), 247405 (2003).
14. M. Lancry, B. Poumellec, J. Canning, K. Cook, J. C. Poulin, and F. Brisset, "Ultrafast nanoporous silica formation driven by femtosecond laser irradiation," Laser Photonics Rev. **7**(6), 953–962 (2013).
15. A. Y. Vorobyev and C. Guo, "Direct femtosecond laser surface nano/microstructuring and its applications," Laser Photonics Rev. **7**(3), 385–407 (2013).
16. J. Bonse, S. Höhm, S. V. Kirner, A. Rosenfeld, and J. Krüger, "Laser-induced periodic surface structures—A scientific evergreen," IEEE J. Sel. Top. Quantum Electron. **23**, 1 (2016).
17. J. Wang and C. Guo, "Ultrafast dynamics of femtosecond laser-induced periodic surface pattern formation on metals," Appl. Phys. Lett. **87**(25), 251914 (2005).
18. I. Gnilitskyi, T. J.-Y. Derrien, Y. Levy, N. M. Bulgakova, T. Mocek, and L. Orazi, "High-speed manufacturing of highly regular femtosecond laser-induced periodic surface structures: Physical origin of regularity," Sci. Rep. **7**(1), 8485 (2017).
19. B. Zhao, J. Yang, J. Cheng, and C. Guo, "Capture of femtosecond plasmon excitation on transient nonequilibrium states of the metal surface," Phys. Rev. Res. **2**(3), 033418 (2020).
20. J. Bonse, S. Baudach, J. Krüger, W. Kautek, and M. Lenzner, "Femtosecond laser ablation of silicon–modification thresholds and morphology," Appl. Phys. A **74**(1), 19–25 (2002).
21. L. Wang, Q.-D. Chen, X.-W. Cao, R. Buividas, X. Wang, S. Juodkazis, and H.-B. Sun, "Plasmonic nano-printing: large-area nanoscale energy deposition for efficient surface texturing," Light: Sci. Appl. **6**(12), e17112 (2017).
22. J. Reif, F. Costache, M. Henyk, and S. V. Pandelov, "Ripples revisited: non-classical morphology at the bottom of femtosecond laser ablation craters in transparent dielectrics," Appl. Surf. Sci. **197-198**, 891–895 (2002).
23. F. Liang, Q. Sun, D. Gingras, R. Vallée, and S. L. Chin, "The transition from smooth modification to nanograting in fused silica," Appl. Phys. Lett. **96**(10), 101903 (2010).
24. S. Höhm, A. Rosenfeld, J. Krüger, and J. Bonse, "Femtosecond laser-induced periodic surface structures on silica," J. Appl. Phys. **112**(1), 014901 (2012).
25. B. Öktem, I. Pavlov, S. Ilday, H. Kalaycıoğlu, A. Rybak, S. Yavaş, M. Erdoğan, and F. Ö. Ilday, "Nonlinear laser lithography for indefinitely large-area nanostructuring with femtosecond pulses," Nat. Photonics **7**(11), 897–901 (2013).

26. K. Cheng, J. Liu, K. Cao, L. Chen, Y. Zhang, Q. Jiang, D. Feng, S. Zhang, Z. Sun, and T. Jia, “Ultrafast dynamics of single-pulse femtosecond laser-induced periodic ripples on the surface of a gold film,” Phys. Rev. B **98**(18), 184106 (2018).
27. T. Zou, B. Zhao, W. Xin, Y. Wang, B. Wang, X. Zheng, H. Xie, Z. Zhang, J. Yang, and C. Guo, “High-speed femtosecond laser plasmonic lithography and reduction of graphene oxide for anisotropic photoresponse,” Light: Sci. Appl. **9**(1), 1 (2020).
28. A. Cerkauskaite, R. Drevinskas, A. Solodar, I. Abdulhalim, and P. G. Kazansky, “Form-birefringence in ITO thin films engineered by ultrafast laser nanostructuring,” ACS Photonics **4**(11), 2944–2951 (2017).
29. R. Drevinskas, M. Beresna, J. Zhang, A. G. Kazanskii, and P. G. Kazansky, “Ultrafast laser-induced metasurfaces for geometric phase manipulation,” Adv. Opt. Mater. **5**(1), 1600575 (2017).
30. S. Richter, C. Miese, S. Döring, F. Zimmermann, M. J. Withford, A. Tünnermann, and S. Nolte, “Laser induced nanogratings beyond fused silica-periodic nanostructures in borosilicate glasses and ULE™,” Opt. Mater. Express **3**(8), 1161 (2013).
31. F. Zimmermann, A. Plech, S. Richter, A. Tünnermann, and S. Nolte, “Ultrashort laser pulse induced nanogratings in borosilicate glass,” Appl. Phys. Lett. **104**(21), 211107 (2014).
32. T. Asai, Y. Shimotsuma, T. Kurita, A. Murata, S. Kubota, M. Sakakura, K. Miura, F. Brisset, B. Poumellec, and M. Lancry, “Systematic control of structural changes in GeO2 glass induced by femtosecond laser direct writing,” J. Am. Ceram. Soc. **98**(5), 1471–1477 (2015).
33. M. Lancry, F. Zimmerman, R. Desmarchelier, J. Tian, F. Brisset, S. Nolte, and B. Poumellec, “Nanogratings formation in multicomponent silicate glasses,” Appl. Phys. B **122**(3), 66 (2016).
34. F. Zhang, A. Cerkauskaite, R. Drevinskas, P. G. Kazansky, and J. Qiu, “Microengineering of optical properties of GeO2 glass by ultrafast laser nanostructuring,” Adv. Opt. Mater. **5**(23), 1700342 (2017).
35. S. Lotarev, S. Fedotov, A. Kurina, A. Lipatiev, and V. Sigaev, “Ultrafast laser-induced nanogratings in sodium germanate glasses,” Opt. Lett. **44**(7), 1564 (2019).
36. Y. Shimotsuma, K. Hirao, J. Qiu, and P. G. Kazansky, “Nano-modification inside transparent materials by femtosecond laser single beam,” Mod. Phys. Lett. B **19**(05), 225–238 (2005).
37. D. Wortmann, J. Gottmann, N. Brandt, and H. Horn-Solle, “Micro-and nanostructures inside sapphire by fs-laser irradiation and selective etching,” Opt. Express **16**(3), 1517 (2008).
38. P. Karpinski, V. Shvedov, W. Krolikowski, and C. Hnatovsky, “Laser-writing inside uniaxially birefringent crystals: fine morphology of ultrashort pulse-induced changes in lithium niobate,” Opt. Express **24**(7), 7456 (2016).
39. F. Zhang, Z. Nie, H. Huang, L. Ma, H. Tang, M. Hao, and J. Qiu, “Self-assembled three-dimensional periodic micro-nano structures in bulk quartz crystal induced by femtosecond laser pulses,” Opt. Express **27**(5), 6442 (2019).
40. R. Brueckner, “Properties and structure of vitreous silica. I,” J. Non-Cryst. Solids **5**(2), 123–175 (1970).
41. S. Pancharatnam, “Generalized theory of interference and its applications,” Proc. Indian Acad. Sci. **44**(6), 398–417 (1956).
42. Z. E. Bomzon, V. Kleiner, and E. Hasman, “Pancharatnam–Berry phase in space-variant polarization-state manipulations with subwavelength gratings,” Opt. Lett. **26**(18), 1424 (2001).
43. Z. E. Bomzon, G. Biener, V. Kleiner, and E. Hasman, “Space-variant Pancharatnam–Berry phase optical elements with computer-generated subwavelength gratings,” Opt. Lett. **27**(13), 1141 (2002).
44. J. Kim, Y. Li, M. N. Miskiewicz, C. Oh, M. W. Kudenov, and M. J. Escuti, “Fabrication of ideal geometric-phase holograms with arbitrary wavefronts,” Optica **2**(11), 958 (2015).
45. M. Khorasaninejad, W. T. Chen, R. C. Devlin, J. Oh, A. Y. Zhu, and F. Capasso, “Metalenses at visible wavelengths: Diffraction-limited focusing and subwavelength resolution imaging,” Science **352**(6290), 1190–1194 (2016).
46. Q. Zhan, “Cylindrical vector beams: from mathematical concepts to applications,” Adv. Opt. Photonics **1**(1), 1 (2009).
47. C. Hernández-García, A. Turpin, J. San Román, A. Picón, R. Drevinskas, A. Cerkauskaite, P. G. Kazansky, C. G. Durfee, and Í. J. Sola, “Extreme ultraviolet vector beams driven by infrared lasers,” Optica **4**(5), 520 (2017).
48. V. Parigi, V. D’Ambrosio, C. Arnold, L. Marrucci, F. Sciarrino, and J. Laurat, “Storage and retrieval of vector beams of light in a multiple-degree-of-freedom quantum memory,” Nat. Commun. **6**(1), 7706 (2015).
49. R. Dorn, S. Quabis, and G. Leuchs, “Sharper focus for a radially polarized light beam,” Phys. Rev. Lett. **91**(23), 233901 (2003).
50. C. Guclu, M. Veysi, and F. Capolino, “Photoinduced magnetic nanoprobe excited by an azimuthally polarized vector beam,” ACS Photonics **3**(11), 2049–2058 (2016).
51. G. Zheng, H. Mühlenbernd, M. Kenney, G. Li, T. Zentgraf, and S. Zhang, “Metasurface holograms reaching 80% efficiency,” Nat. Nanotechnol. **10**(4), 308–312 (2015).
52. M. N. Miskiewicz and M. J. Escuti, “Direct-writing of complex liquid crystal patterns,” Opt. Express **22**(10), 12691 (2014).
53. M. Beresna, M. Gecevičius, P. G. Kazansky, and T. Gertus, “Radially polarized optical vortex converter created by femtosecond laser nanostructuring of glass,” Appl. Phys. Lett. **98**(20), 201101 (2011).
54. X. Ling, X. Zhou, X. Yi, W. Shu, Y. Liu, S. Chen, H. Luo, S. Wen, and D. Fan, “Giant photonic spin Hall effect in momentum space in a structured metamaterial with spatially varying birefringence,” Light: Sci. Appl. **4**(5), e290 (2015).

55. J. Zhang, M. Gecevicius, M. Beresna, and P. G. Kazansky, "Seemingly unlimited lifetime data storage in nanostructured glass," Phys. Rev. Lett. **112**(3), 033901 (2014).
56. J. H. Strickler and W. W. Webb, "Three-dimensional optical data storage in refractive media by two-photon point excitation," Opt. Lett. **16**(22), 1780 (1991).
57. R. Imai, M. Shiozawa, T. Shintani, T. Watanabe, S. Mori, Y. Shimotsuma, M. Sakakura, K. Miura, and K. Watanabe, "100-Layer recording in fused silica for semi permanent data storage," Jpn. J. Appl. Phys. **54**(9S), 09MC02 (2015).
58. A. Royon, K. Bourhis, M. Bellec, G. Papon, B. Bousquet, Y. Deshayes, T. Cardinal, and L. Canioni, "Silver clusters embedded in glass as a perennial high capacity optical recording medium," Adv. Mater. **22**(46), 5282–5286 (2010).
59. P. Zijlstra, J. W. Chon, and M. Gu, "Five-dimensional optical recording mediated by surface plasmons in gold nanorods," Nature **459**(7245), 410–413 (2009).
60. X. Ouyang, Y. Xu, Z. Feng, W. Tang, Y. Cao, and X. Li, "Polychromatic and polarized multilevel optical data storage," Nanoscale **11**(5), 2447–2452 (2019).
61. M. Xian, Y. Xu, X. Ouyang, Y. Cao, S. Lan, and X. Li, "Segmented cylindrical vector beams for massively-encoded optical data storage," Sci. Bull. **65**(24), 2072–2079 (2020).
62. X. Ouyang, Y. Xu, M. Xian, Z. Feng, L. Zhu, Y. Cao, S. Lan, B.-O. Guan, C.-W. Qiu, and M. Gu, "Synthetic helical dichroism for six-dimensional optical orbital angular momentum multiplexing," Nat. Photonics **15**(12), 901–907 (2021).
63. Y. Shimotsuma, M. Sakakura, P. G. Kazansky, M. Beresna, J. Qiu, K. Miura, and K. Hirao, "Ultrafast manipulation of self-assembled form birefringence in glass," Adv. Mater. **22**(36), 4039–4043 (2010).
64. M. Beresna, M. Gecevičius, P. G. Kazansky, T. Taylor, and A. V. Kavokin, "Exciton mediated self-organization in glass driven by ultrashort light pulses," Appl. Phys. Lett. **101**(5), 053120 (2012).
65. R. Drevinskas and P. G. Kazansky, "High-performance geometric phase elements in silica glass," APL Photonics **2**(6), 066104 (2017).
66. M. Sakakura, Y. Lei, L. Wang, Y. H. Yu, and P. G. Kazansky, "Ultralow-loss geometric phase and polarization shaping by ultrafast laser writing in silica glass," Light: Sci. Appl. **9**(1), 15 (2020).
67. H. Wang, Y. Lei, L. Wang, M. Sakakura, Y. Yu, G. Shayeganrad, and P. G. Kazansky, "100-Layer Error-Free 5D Optical Data Storage by Ultrafast Laser Nanostructuring in Glass," Laser Photonics Rev. **16**(4), 2100563 (2022).
68. Y. Lei, M. Sakakura, L. Wang, Y. Yu, H. Wang, G. Shayeganrad, and P. G. Kazansky, "High speed ultrafast laser anisotropic nanostructuring by energy deposition control via near-field enhancement," Optica **8**(11), 1365 (2021).
69. K. M. Davis, K. Miura, N. Sugimoto, and K. Hirao, "Writing waveguides in glass with a femtosecond laser," Opt. Lett. **21**(21), 1729 (1996).
70. K. Miura, J. Qiu, H. Inouye, T. Mitsuyu, and K. Hirao, "Photowritten optical waveguides in various glasses with ultrashort pulse laser," Appl. Phys. Lett. **71**(23), 3329–3331 (1997).
71. D. Homoelle, S. Wielandy, A. L. Gaeta, N. F. Borrelli, and C. Smith, "Infrared photosensitivity in silica glasses exposed to femtosecond laser pulses," Opt. Lett. **24**(18), 1311–1313 (1999).
72. E. N. Glezer and E. Mazur, "Ultrafast-laser driven micro-explosions in transparent materials," Appl. Phys. Lett. **71**(7), 882–884 (1997).
73. S. M. Eaton, W. Chen, L. Zhang, H. Zhang, R. Iyer, J. Aitchison, and P. Herman, "Telecom-band directional coupler written with femtosecond fiber laser," IEEE Photonics Technol. Lett. **18**(20), 2174–2176 (2006).
74. K. Sugioka and Y. Cheng, "Femtosecond laser processing for optofluidic fabrication," Lab Chip **12**(19), 3576 (2012).
75. A. Crespi, R. Osellame, R. Ramponi, D. J. Brod, E. F. Galvao, N. Spagnolo, C. Vitelli, E. Maiorino, P. Mataloni, and F. Sciarrino, "Integrated multimode interferometers with arbitrary designs for photonic boson sampling," Nat. Photonics **7**(7), 545–549 (2013).
76. S. Juodkazis, H. Misawa, T. Hashimoto, E. G. Gamaly, and B. Luther-Davies, "Laser-induced microexplosion confined in a bulk of silica: Formation of nanovoids," Appl. Phys. Lett. **88**(20), 201909 (2006).
77. S. Juodkazis, K. Nishimura, S. Tanaka, H. Misawa, E. G. Gamaly, B. Luther-Davies, L. Hallo, P. Nicolai, and V. T. Tikhonchuk, "Laser-induced microexplosion confined in the bulk of a sapphire crystal: evidence of multimegabar pressures," Phys. Rev. Lett. **96**(16), 166101 (2006).
78. S. Kanehira, J. Si, J. Qiu, K. Fujita, and K. Hirao, "Periodic nanovoid structures via femtosecond laser irradiation," Nano Lett. **5**(8), 1591–1595 (2005).
79. X. Hu, B. Qian, P. Zhang, X. Wang, L. Su, J. Qiu, and C. Zhu, "Self-organized microvoid array perpendicular to the femtosecond laser beam in CaF2 crystals," Laser Phys. Lett. **5**(5), 394–397 (2008).
80. M. Terakawa, E. Toratani, T. Shirakawa, and M. Obara, "Fabrication of a void array in dielectric materials by femtosecond laser micro-processing for compact photonic devices," Appl. Phys. A **100**(4), 1041–1047 (2010).
81. P. Vlugter and Y. Bellouard, "Elastic properties of self-organized nanogratings produced by femtosecond laser exposure of fused silica," Phys. Rev. Mater. **4**(2), 023607 (2020).
82. V. R. Bhardwaj, E. Simova, P. P. Rajeev, C. Hnatovsky, R. S. Taylor, D. M. Rayner, and P. B. Corkum, "Optically produced arrays of planar nanostructures inside fused silica," Phys. Rev. Lett. **96**(5), 057404 (2006).
83. R. Taylor, C. Hnatovsky, E. Simova, P. Rajeev, D. Rayner, and P. Corkum, "Femtosecond laser erasing and rewriting of self-organized planar nanocracks in fused silica glass," Opt. Lett. **32**(19), 2888 (2007).

84. W. Zhang, Q. Zhai, J. Song, K. Lou, Y. Li, Z. Ou, Q. Zhao, and Y. Dai, "Manipulation of self-organized nanograting for erasing and rewriting by ultrashort double-pulse sequences irradiation in fused silica," J. Phys. D: Appl. Phys. **53**(16), 165106 (2020).
85. E. Bricchi and P. G. Kazansky, "Extraordinary stability of anisotropic femtosecond direct-written structures embedded in silica glass," Appl. Phys. Lett. **88**(11), 111119 (2006).
86. Y. Wang, M. Cavillon, N. Ollier, B. Poumellec, and M. Lancry, "An Overview of the Thermal Erasure Mechanisms of Femtosecond Laser-Induced Nanogratings in Silica Glass," Phys. Status Solidi A **218**(12), 2100023 (2021).
87. T. Tsai and D. Griscom, "Experimental evidence for excitonic mechanism of defect generation in high-purity silica," Phys. Rev. Lett. **67**(18), 2517–2520 (1991).
88. P. N. Saeta and B. I. Greene, "Primary relaxation processes at the band edge of SiO2," Phys. Rev. Lett. **70**(23), 3588–3591 (1993).
89. L. Skuja, B. Güttler, D. Schiel, and A. Silin, "Infrared photoluminescence of preexisting or irradiation-induced interstitial oxygen molecules in glassy SiO2 and α-quartz," Phys. Rev. B **58**(21), 14296–14304 (1998).
90. K. Mishchik, C. d'Amico, P. K. Velpula, C. Mauclair, A. Boukenter, Y. Ouerdane, and R. Stoian, "Ultrafast laser induced electronic and structural modifications in bulk fused silica," J. Appl. Phys. **114**(13), 133502 (2013).
91. Y. Bellouard, A. Champion, B. McMillen, S. Mukherjee, R. R. Thomson, C. Pépin, P. Gillet, and Y. Cheng, "Stress-state manipulation in fused silica via femtosecond laser irradiation," Optica **3**(12), 1285 (2016).
92. R. Stoian, K. Mishchik, G. Cheng, C. Mauclair, C. D'Amico, J.-P. Colombier, and M. Zamfirescu, "Investigation and control of ultrafast laser-induced isotropic and anisotropic nanoscale-modulated index patterns in bulk fused silica," Opt. Mater. Express **3**(10), 1755 (2013).
93. B. C. Stuart, M. D. Feit, A. M. Rubenchik, B. W. Shore, and M. D. Perry, "Laser-induced damage in dielectrics with nanosecond to subpicosecond pulses," Phys. Rev. Lett. **74**(12), 2248–2251 (1995).
94. N. M. Bulgakova, V. P. Zhukov, S. V. Sonina, and Y. P. Meshcheryakov, "Modification of transparent materials with ultrashort laser pulses: What is energetically and mechanically meaningful?" J. Appl. Phys. **118**(23), 233108 (2015).
95. D. Rayner, A. Naumov, and P. Corkum, "Ultrashort pulse non-linear optical absorption in transparent media," Opt. Express **13**(9), 3208 (2005).
96. A. Rudenko, J. P. Colombier, T. E. Itina, and R. Stoian, "Genesis of Nanogratings in Silica Bulk via Multipulse Interplay of Ultrafast Photo-Excitation and Hydrodynamics," Adv. Opt. Mater. **9**(20), 2100973 (2021).
97. Y. Liao, Y. Shen, L. Qiao, D. Chen, Y. Cheng, K. Sugioka, and K. Midorikawa, "Femtosecond laser nanostructuring in porous glass with sub-50 nm feature sizes," Opt. Lett. **38**(2), 187 (2013).
98. R. Buschlinger, S. Nolte, and U. Peschel, "Self-organized pattern formation in laser-induced multiphoton ionization," Phys. Rev. B **89**(18), 184306 (2014).
99. A. Rudenko, J.-P. Colombier, and T. E. Itina, "From random inhomogeneities to periodic nanostructures induced in bulk silica by ultrashort laser," Phys. Rev. B **93**(7), 075427 (2016).
100. M. Shimizu, M. Sakakura, M. Ohnishi, Y. Shimotsuma, T. Nakaya, K. Miura, and K. Hirao, "Mechanism of heat-modification inside a glass after irradiation with high-repetition rate femtosecond laser pulses," J. Appl. Phys. **108**(7), 073533 (2010).
101. T. Zou, B. Zhao, W. Xin, F. Wang, H. Xie, Y. Li, Y. Shan, K. Li, Y. Sun, and J. Yang, "Birefringent response of graphene oxide film structurized via femtosecond laser," Nano. Research. **1**, 4490 (2021).
102. S. Liu, K. Switkowski, C. Xu, J. Tian, B. Wang, P. Lu, W. Krolikowski, and Y. Sheng, "Nonlinear wavefront shaping with optically induced three-dimensional nonlinear photonic crystals," Nat. Commun. **10**(1), 1 (2019).
103. D. Wei, C. Wang, H. Wang, X. Hu, D. Wei, X. Fang, Y. Zhang, D. Wu, Y. Hu, and J. Li, "Experimental demonstration of a three-dimensional lithium niobate nonlinear photonic crystal," Nat. Photonics **12**(10), 596–600 (2018).
104. T. Xu, K. Switkowski, X. Chen, S. Liu, K. Koynov, H. Yu, H. Zhang, J. Wang, Y. Sheng, and W. Krolikowski, "Three-dimensional nonlinear photonic crystal in ferroelectric barium calcium titanate," Nat. Photonics **12**(10), 591–595 (2018).
105. X. Huang, Q. Guo, D. Yang, X. Xiao, X. Liu, Z. Xia, F. Fan, J. Qiu, and G. Dong, "Reversible 3D laser printing of perovskite quantum dots inside a transparent medium," Nat. Photonics **14**(2), 82–88 (2020).
106. J. Cao, B. Poumellec, L. Mazerolles, F. Brisset, A. L. Helbert, S. Surble, X. He, and M. Lancry, "Nanoscale phase separation in lithium niobium silicate glass by femtosecond laser irradiation," J. Am. Ceram. Soc. **100**(1), 115–124 (2017).
107. J. Cao, M. Lancry, F. Brisset, L. Mazerolles, R. Saint-Martin, and B. Poumellec, "Femtosecond laser-induced crystallization in glasses: growth dynamics for orientable nanostructure and nanocrystallization," Cryst. Growth Des. **19**(4), 2189–2205 (2019).
108. B. Zhang, Z. Wang, D. Tan, X. Liu, B. Xu, L. Tong, P. G. Kazansky, and J. Qiu, "Ultrafast Laser Inducing Continuous Periodic Crystallization in the Glass Activated via Laser-Prepared Crystallite-Seeds," Adv. Opt. Mater. **9**(8), 2001962 (2021).
109. B. Zhang, D. Tan, Z. Wang, X. Liu, B. Xu, M. Gu, L. Tong, and J. Qiu, "Self-organized phase-transition lithography for all-inorganic photonic textures," Light: Sci. Appl. **10**(1), 1 (2021).
110. E. Maguid, I. Yulevich, M. Yannai, V. Kleiner, M. L Brongersma, and E. Hasman, "Multifunctional interleaved geometric-phase dielectric metasurfaces," Light: Sci. Appl. **6**(8), e17027 (2017).
111. P. Gotovski, P. Šlevas, E. Nacius, V. Jukna, S. Orlov, O. Ulcinas, J. Baltrukonis, and T. Gertus, "Design of efficient Gauss to top-hat converters using geometrical phase elements inscribed in the glass by femtosecond laser pulses," in

Laser Resonators, Microresonators, and Beam Control XXII (International Society for Optics and Photonics, 2020), 112661J.

112. P. Gotovski, P. Šlevas, E. Nacius, V. Jukna, S. Orlov, J. Baltrukonis, O. Ulčinas, and T. Gertus, "Formation of optical needles by Pancharatnam-Berry phase element for laser-induced modifications in transparent materials," in *Laser-based Micro-and Nanoprocessing XIV*, (International Society for Optics and Photonics, 2020), 112681Y.
113. X. Chang, Y. Lei, H. Wang, G. Shayeganrad, C. Deng, and P. Kazansky, "High Damage Threshold Ultrafast Laser Nanostructuring in Silica Glass," in *2021 Conference on Lasers and Electro-Optics Europe & European Quantum Electronics Conference (CLEO/Europe-EQEC)*, (IEEE, 2021), 1.
114. D. Coursault and E. Brasselet, "Nanostructured silica spin–orbit optics for modal vortex beam shaping," Nanophotonics **11**(4), 805–812 (2022).
115. T. Jefferson-Brain, Y. Lei, P. Kazansky, and W. Clarkson, "Generation of a Radially Polarised Beam in a Solid-State Laser Using an Intracavity Spatially Variant Waveplate," in *2021 Conference on Lasers and Electro-Optics Europe & European Quantum Electronics Conference (CLEO/Europe-EQEC)*, (IEEE, 2021), 1.
116. A. S. Lipatiev, S. S. Fedotov, A. G. Okhrimchuk, S. V. Lotarev, A. M. Vasetsky, A. A. Stepko, G. Y. Shakhgildyan, K. I. Piyanzina, I. S. Glebov, and V. N. Sigaev, "Multilevel data writing in nanoporous glass by a few femtosecond laser pulses," Appl. Opt. **57**(4), 978 (2018).
117. S. Fedotov, A. Okhrimchuk, A. Lipatiev, A. Stepko, K. Piyanzina, G. Y. Shakhgildyan, M. Y. Presniakov, I. Glebov, S. Lotarev, and V. Sigaev, "3-bit writing of information in nanoporous glass by a single sub-microsecond burst of femtosecond pulses," Opt. Lett. **43**(4), 851 (2018).
118. S. Fedotov, A. Lipatiev, M. Y. Presniakov, G. Y. Shakhgildyan, A. Okhrimchuk, S. Lotarev, and V. Sigaev, "Laser-induced cavities with a controllable shape in nanoporous glass," Opt. Lett. **45**(19), 5424 (2020).
119. Z. Yan, J. Gao, M. Beresna, and J. Zhang, "Near-Field Mediated 40 nm In-Volume Glass Fabrication by Femtosecond Laser," Adv. Opt. Mater. **10**(4), 2101676 (2021).
120. Z. Yan, P. Li, J. Gao, Y. Wang, L. Wang, M. Beresna, and J. Zhang, "Anisotropic nanostructure generated by a spatial-temporal manipulated picosecond pulse for multidimensional optical data storage," Opt. Lett. **46**(21), 5485 (2021).